

## ARTICLE

### Data-driven discovery of the equations of turbulent convection

Christopher J. Wareing<sup>†\*</sup>, Alasdair T. Roy<sup>†</sup>, Matthew Golden<sup>‡</sup>, Roman O. Grigoriev<sup>‡</sup>, and Steven M. Tobias<sup>†</sup>

<sup>†</sup> Department of Applied Mathematics, School of Mathematics, University of Leeds, Leeds, LS2 9JT, UK

<sup>‡</sup> School of Physics, Georgia Institute of Technology, North Avenue, Atlanta, GA 30332, USA

(*recv. 2024 November 14; acc. 2025 May 14*)

We compare the efficiency and ease-of-use of the Sparse Identification of Nonlinear Dynamics (SINDy) algorithm and Sparse Physics-Informed Discovery of Empirical Relations (SPIDER) framework in recovering the relevant governing equations and boundary conditions from data generated by direct numerical simulations (DNS) of turbulent convective flows. In the former case, a weak-form implementation pySINDy is used. Time-dependent data for two- (2D) and three-dimensional (3D) DNS simulation of Rayleigh-Bénard convection and convective plane Couette flow is generated using the Dedalus PDE framework for spectrally solving differential equations. Using pySINDy we are able to recover the governing equations of 2D models of Rayleigh-Bénard convection at Rayleigh numbers,  $R$ , from laminar, through transitional to moderately turbulent flow conditions, albeit with increasing difficulty with larger Rayleigh number, especially in recovery of the diffusive terms (with coefficient magnitude proportional to  $\sqrt{1/R}$ ). SPIDER requires a much smaller library of terms and we are able to recover more easily the governing equations for a wider range of  $R$  in 2D and 3D convection and plane flow models and go on to recover constraints (the incompressibility condition) and boundary conditions, demonstrating the benefits and capabilities of SPIDER to go beyond pySINDy for these fluid problems governed by second-order PDEs. At the highest values of  $R$ , discrepancies appear between the governing equations that are solved and those that are discovered by SPIDER. We find that this is likely associated with limited resolution of DNS, demonstrating the potential of machine-learning methods to validate numerical solvers and solutions for such flow problems. We also find that properties of the flow, specifically the correlation time and spatial scales, should inform the initial selection of spatiotemporal subdomain sizes for both pySINDy and SPIDER. Adopting this default position has the potential to reduce trial and error in selection of data parameters, saving considerable time and effort and allowing the end user of these or similar methods to focus on the importance of setting the power of the integrating polynomial in these weak-form methods and the tolerance of the optimiser technique selected.

**Keywords:** Boundary conditions; Navier Stokes equations; machine learning; data-driven techniques; sparse regression

## 1. Introduction

Geophysical and astrophysical flows are characterised by their nonlinear interaction over a vast range of spatial and temporal scales and hence the presence of turbulence. Often this turbulence is inhomogeneous and anisotropic owing to the nature of the driving (and possibly the presence of rotation, stratification and mean flows) (Marston and Tobias 2023). The large range of scales often requires the modelling of scales that are not captured by the numerical solution, sometimes denoted as subgrid modelling. As recently reviewed in Moser, Haering & Yalla (2021) this can take many forms, including the derivation of statistical representations of the unresolved scales (e.g. Chorin, Hald & Kupferman (2002)), utilising machine learning to replicate the response of the unresolved scales (Bolton and Zanna 2019, Zanna and Bolton

---

\*Corresponding author. Email: C.J.Wareing@leeds.ac.uk

2020) or discovering the effective equations satisfied by the low-order statistics of those scales. These ‘turbulent closure equations’ or parameterisations of the turbulent transport coefficients are the subject of much ongoing cutting-edge research; see the summary in Jakhar *et al.* (2024).

In this paper, as a first step to test the methods that we intend in future work to apply to the search for turbulent closure models (such as Garaud *et al.* 2010), we focus on the simpler problem of the reconstruction of the relevant full underlying equations from data. This problem is easier because it does not rely on assuming the correct definition of an averaging procedure or maintaining realisability of the reconstructed equations. Here we are interested in how two leading equation inference methods perform for a turbulent flow driven by buoyancy (and, in some cases, driven from the boundaries). This form of driving is important in many geophysical and astrophysical settings where thermal convection is responsible for heat (and possibly momentum) transport in planets and stars.

Whilst recovery of evolution equations via some form of regression is now common, with the Sparse Identification of Nonlinear Dynamics (SINDy) algorithm (Brunton, Proctor & Kutz 2016) so far proven to be the default choice of approach, identification of flow constraints and boundary conditions from data - simulated or experimental - is still relatively rare. Reduction techniques and regressive reconstruction, using neural networks, have been shown to be able to reconstruct the latent fluid state for a number of unsteady flows, e.g. vortex shedding at Reynolds numbers up to 20000 (Dubois *et al.* 2022). Similarly, artificial neural networks have been trained to solve a non-linear regression problem and obtain inlet conditions for a fluid flow problem; see V  ras *et al.* (2021) and citations of this paper using this strategy. As far as we are aware, sparse regression machine-learning techniques have only recently been shown as able to recover equations of flow constraints and boundary conditions through the Sparse Physics-Informed Discovery of Empirical Relations (SPIDER) framework (Gurevich *et al.* 2024).

In this paper, as a first step toward turbulence closure model recovery, we apply both SINDy and SPIDER to convective flow problems. The goal is to compare their performance and relative merits and look to provide guidance for the end-user of either technique. This paper is organised as follows: In Section 2, we present the convection models we have considered. In Section 3 we obtain simulated data of these models using spectral methods. We introduce and compare the two equation discovery methods, noting their similar objectives and highlighting the differences in application in Section 4. We explore the equation recovery performance of both methods in Section 5 and discuss the limitations, possible reasons for the differences and some advice for future users of either machine-learning approach in Section 6. Finally, we summarise this work and look to future directions in Section 7.

## 2. Models

### 2.1. Rayleigh-B  nard convection

We consider classical Rayleigh-B  nard convective fluid flow in a flat horizontally-periodic layer heated from below. We assume the Boussinesq approximation. The non-dimensionalized dynamical equations for the fluid are

$$\frac{\partial \mathbf{u}}{\partial t} + (\mathbf{u} \cdot \nabla) \mathbf{u} = -\nabla p + T \hat{\mathbf{z}} + \sqrt{\frac{P}{R}} \nabla^2 \mathbf{u}, \quad (1a)$$

$$\frac{\partial T}{\partial t} + (\mathbf{u} \cdot \nabla) T = \frac{1}{\sqrt{R P}} \nabla^2 T, \quad (1b)$$

$$\nabla \cdot \mathbf{u} = 0, \quad (1c)$$

where the non-dimensional fields are  $\mathbf{u}$ , the vector velocity field, the scalar pressure field  $p$  and the scalar temperature field  $T$ . Here the non-dimensional parameters are the Rayleigh number  $R = \alpha g(\Delta T)L^3/\nu\kappa$  and the Prandtl number  $P = \nu/\kappa$ . Gravity acts in the  $-\hat{z}$  direction and  $\alpha$ ,  $\kappa$  and  $\nu$  are the thermal heat expansion coefficient, thermal diffusivity and kinematic viscosity respectively,  $g$  is the acceleration due to gravity,  $L$  is the vertical height of the layer, and  $\Delta T$  is the temperature difference between the bottom and top plates.

For the non-dimensionalization we have used  $L$  as the length-scale, the buoyancy free-fall velocity  $(\sqrt{\alpha g(\Delta T)L})$  as the velocity scale, and  $\Delta T$  as the temperature scale. As a consequence,  $L/\sqrt{\alpha g(\Delta T)L}$  is the time-scale. We consider both two-dimensional and three-dimensional cases. We use an aspect ratio of four for the layer, such that for the 2D simulations the layer is four times longer in the  $x$  direction than in the buoyancy direction of  $z$ , and for the 3D simulations the layer is four times longer in both the  $x$  and  $y$  directions than in the vertical  $z$  direction, defined as the one opposite to gravity. We confine ourselves in this study to Prandtl number  $P = 1$ .

We impose the stress-free, isothermal, boundary condition on the problem, such that fluid conditions on the top ( $z = 1$ ) and bottom ( $z = 0$ ) boundaries satisfy the following relations as necessary depending on the number of dimensions

$$\frac{\partial u_x}{\partial z} = 0, \quad (2a)$$

$$\frac{\partial u_y}{\partial z} = 0, \quad (2b)$$

$$u_z = 0, \quad (2c)$$

$$T(z = 0) = 1, \quad (2d)$$

$$T(z = 1) = 0. \quad (2e)$$

## 2.2. Planar convective Couette flow

In this 2D model of planar convective Couette flow, we extend the model of Rayleigh-Bénard convection above to move the top and bottom boundaries in antiparallel directions, such that the non-dimensionalized dynamical equations and the boundary condition on the temperature remain unchanged, but the boundary condition on the velocity is now that of the no-slip condition

$$u_z(z = 0) = 0, \quad (3a)$$

$$u_z(z = 1) = 0, \quad (3b)$$

$$u_x(z = 0) = -U_0, \quad (3c)$$

$$u_x(z = 1) = U_0, \quad (3d)$$

while the boundary condition on the temperature remains unchanged.  $U_0$  therefore represents the velocity on the the walls measured in units of the free-fall velocity. The vertical height and aspect ratio of the problem remain the same, resulting in a physical extent of  $4 \times 1$  in this 2D problem.

### 3. Numerical method and Resolution

The above models are solved numerically for a Cartesian geometry using the Dedalus framework for solving partial differential equations using spectral methods, specifically version 3.0.1<sup>1</sup> (Burns *et al.* 2020). The 2D model of Rayleigh-Bénard convection closely follows that of the 2D initial value problem (IVP) in the Cartesian examples packaged in the examples sub-directory of the Dedalus3 code repository, except that the stress-free, rather than no-slip, boundary condition is imposed on the problem. Furthermore, rather than the second-order, two-stage DIRK+ERK (d3.RK222) timestepping scheme (Ascher *et al.* 1997 sec. 2.6), we use the third-order, four-stage DIRK+ERK (d3.RK443) scheme (Ascher *et al.* 1997 sec. 2.8) for greater accuracy and stability.

We use a periodic Fourier basis for the  $x$  and  $y$  directions, and a Chebyshev basis for the  $z$  direction. In all bases, a Dedalus dealiasing factor of  $3/2$  (equivalent to the conventional  $2/3$ ) is employed. Scalar fields are defined for pressure and temperature and a vector field for velocity. The *generalised tau method* is used for imposing boundary conditions; explicit tau terms are added to the PDE introducing degrees of freedom that allow the problem to be solved exactly over polynomials. Further details can be obtained from the Dedalus repository<sup>1</sup> and in the Dedalus methods paper (Burns *et al.* 2020).

Our simulations use a Courant-Friedrichs-Lewy solver (d3.CFL) with an initial and maximum timestep set to 0.01, a safety factor (the Courant number) of 0.5, an iteration cadence of 10 for calculating a new timestep, a maximum and minimum fractional change between timesteps of 1.5 and 0.5 respectively and a fractional change threshold for changing the timestep of 0.05. We have not explored variation of these parameters.

We monitor Reynolds number, Nusselt number, average kinetic energy and total kinetic energy in order to decide when a statistically steady state has been reached. We arbitrarily select this regime for the application of machine learning methods, but one could examine the ability in other more transient periods of the flow.

It is common knowledge that, in order for a data-driven approach to recover a mathematical model, the data must exhibit enough variation on both space and time to sample the state of the physical problem (Schaeffer *et al.* 2018). For this reason, we employ a constant high resolution for each instance of the Rayleigh number, as detailed in this section. The use of the same resolution for all, defined so as to resolve the turbulent evolution and structure at the largest  $R$ , may seem over-resolved and numerically expensive, but tests show there are no detrimental effects compared to lower resolutions and all run to a statistically steady state in a matter of hours at most on single 40-core blades of the HPC resources for the 2D problem and ten 40-core blades for the 3D problem. We include our Dedalus scripts for all the models studied in the data repository accompanying this paper for reproducibility and replicability<sup>1</sup>.

#### 3.1. 2D Rayleigh-Bénard convection

In two dimensions, we perform simulations for Rayleigh numbers  $R = 10^6$ ,  $10^8$ ,  $10^{10}$  and  $10^{12}$ , modelling the laminar, transitional and turbulent regimes, as confirmed by monitoring of the Nusselt and Reynolds numbers. The physical domain is discretized into a uniform grid of 1024 points in the  $x$  direction and 384 non-uniform points in the  $z$  direction defined by the Chebyshev basis. The Chebyshev basis allows for more accurate resolution of the boundary layers than a uniformly spaced grid of 384 points. This vertical resolution places a similar number of grid points in the boundary layer compared to other DNS studies of the same problem (Zhu *et al.* 2018). Power spectra of the whole flow also demonstrate that the steep

<sup>1</sup><https://github.com/DedalusProject/dedalus/releases/tag/v3.0.1>

<sup>1</sup><https://doi.org/10.5518/1577>

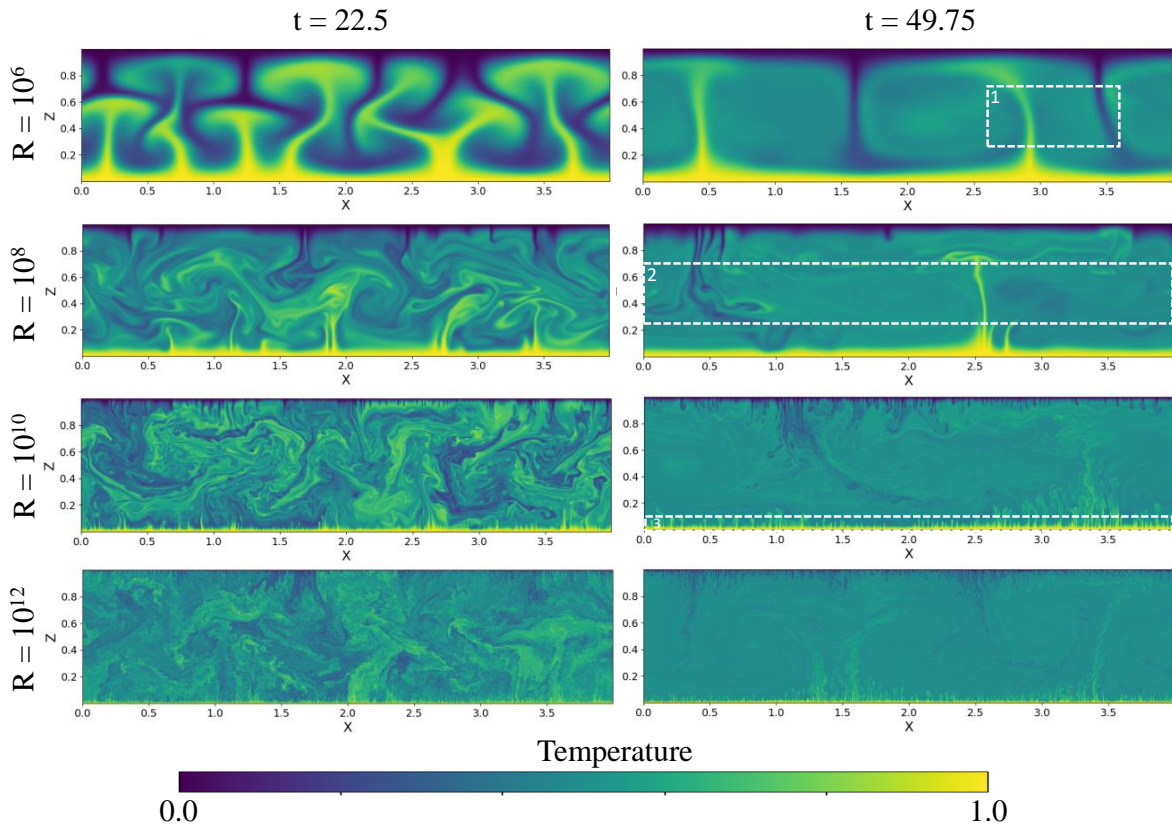


Figure 1. Snapshots of 2D Rayleigh-Bénard convection at varying times and Rayleigh number. Snapshots are shown early in the initial evolution ( $t = 22.5$  in the left column) and once the steady state has become established ( $t = 49.75$  in the right column). Boxes indicated by numbers 1, 2 and 3 overlaid in the right column show the approximate sample domains for the various pySINDy tests discussed in Section 5.

drop off in power at small scales is fully captured at this resolution for  $R$  values of  $10^6$  and  $10^8$ , but then approaching the limit at  $10^{10}$  and at the limit for  $10^{12}$ . We return to the importance of resolution and how this may be affecting the methods in later discussions.

The initial physical values of the scalar pressure field and components of the vector velocity field are all set to zero. The physical temperature (buoyancy) field is filled with random noise on a normal distribution curve with a magnitude of  $10^{-5}$ . The noise is damped at the walls according to  $T(z) \rightarrow T(z) \times z \times (L - z)$  and a linear background is imposed  $T(z) = T(z) + (L - z)$ .

The simulations are evolved until a time  $t = 50$ , which our investigations have shown is the time at which all simulations have reached an approximately steadily evolving saturated state. Note that some simulations, with lower Rayleigh numbers, reach a steadily evolving state of convective rolls sooner, as is to be expected. At  $t = 50$  the Dedalus model is restarted and evolved until  $t = 60$  with the state of the fluid checkpointed at a much higher cadence,  $\Delta t = 0.01$ , in order to provide the resolution in time required for the machine learning approaches. We show snapshots of the temperature for a range of parameters in Figure 1.

### 3.2. 3D Rayleigh Bénard convection

In three dimensions, we perform simulations for Rayleigh numbers  $R = 10^4$ ,  $10^5$ ,  $10^6$  and  $10^7$ , again modelling the same range of fluid regimes and monitored by Nusselt and Reynolds numbers. The physical domain is discretized into uniform grids of 128 points in the  $x$  and  $y$  directions and 192 non-uniform points in the  $z$  direction defined by the Chebyshev basis.

The initial values of the fields are generated in the same manner as in the 2D model but

here the simulations are evolved considerably further to a time of  $t = 150$  in order to reach a statistically steady state, before restarting and evolving the simulation up to  $t = 175$  in order to obtain snapshots of the fluid state at the smaller interval of  $\Delta t = 0.01$  to provide high cadence snapshots of the fluid for the machine learning algorithms.

### 3.3. Two-dimensional planar convective Couette flow

We perform simulations for the Rayleigh number  $R = 10^8$ , principally to examine the capability of machine learning methods for recovering a boundary condition involving a moving boundary. The physical domain is discretized into a uniform grid of 1024 points in the  $x$  direction and 384 non-uniform points in the  $z$  direction defined by the Chebyshev basis. The initial values of the fields are again generated in the same manner as in the 2D Rayleigh-Bénard convection model, with vertical boundary velocities of  $U_0 = 0.5$  and  $1.0$ . The simulations are evolved up to  $t = 150$  and then restarted in order to obtain fluid data at the same smaller interval of  $\Delta t = 0.01$ , up to  $t = 160$ .

## 4. Equation discovery methods

In this section we introduce the equation discovery algorithms and methods we have used, along with precise details of how we have applied them to the data obtained above. The methods we use are the pySINDy implementation of the Sparse Identification of Nonlinear Dynamics (SINDy) algorithm and the Sparse Physics-Informed Discovery of Empirical Relations (SPIDER) framework. For a recent review of machine learning for PDEs with pySINDy see Brunton & Kutz (2023) and the references therein. The application of the SPIDER algorithm to turbulent channel flow (Gurevich *et al.* 2024) also provides a wide introduction to the history and application of machine learning to PDEs. For reproducibility and completeness, we include our pySINDy and SPIDER analysis scripts, as well as the instances of the libraries used, in the repository accompanying this paper<sup>1</sup>.

### 4.1. The SINDy algorithm

Model discovery is an active field of research which aims to discover models of systems and can find first-principles equations that govern such systems by using observational data. SINDy (Brunton, Proctor & Kutz 2016) has become a popular approach to this problem as it allows the discovery of sparse models which represent the data with a method that is both fast and simple to implement. For this reason SINDy has seen many extensions, such as: implicit equation identification (Kaheman *et al.* 2020), latent space dynamics (Champion *et al.* 2019, Gao & Kutz 2024), globally stable models (Kaptanoglu *et al.* 2021) and rapid-Bayesian formulations (Fung *et al.* 2024). It has since been made available publicly in an open-source Python package called pySINDy (de Silva *et al.* 2021) as a generalisable framework for solving sparse regression problems featuring many of these extensions.

To formulate the optimisation problem in pySINDy, we aim to produce a linear combination of candidate features from a library of terms which generates the dynamics. Explicitly, given  $n$  measurements of a  $d$  dimensional problem, we can construct a state matrix  $\mathbf{X} \in \mathbb{R}^{n \times d}$  where the columns  $j \in [0, 1, \dots, d]$  of  $\mathbf{X}$  represent the state variables and the rows  $i \in [0, 1, \dots, n]$  give measurements in time for each state. The regression problem is cast by solving

$$\dot{\mathbf{X}}_j = \mathbf{\Theta}(\mathbf{X})\xi_j \quad (4)$$

<sup>1</sup><https://doi.org/10.5518/1577>

where  $\Theta \in \mathbb{R}^{n \times p}$  is a feature library constructed of  $p$  terms,  $\xi_j$  is the coefficient vector for the state variable  $j$  and  $\dot{\mathbf{X}}_j$  is the time-derivative of the state variable. The feature library can then be constructed from any terms the user wishes to include, such as polynomial terms of the input states.

Following its introduction, the SINDy algorithm was later extended to learn PDEs from data in the PDE-FIND algorithm (Rudy *et al.* 2017). Given some spatiotemporal data, the extension from ODE to PDE identification is simple. For a general PDE of the form

$$\partial_t \mathbf{u} = \sum_{l=0}^N c_l \mathbf{f}_l(\mathbf{u}, \partial_t \mathbf{u}, \partial_t^2 \mathbf{u}, \nabla \mathbf{u}, \nabla^2 \mathbf{u}, \dots) = 0 \quad (5)$$

where  $c_l$  is the coefficient of  $\mathbf{f}_l$ , we construct a state matrix  $\mathbf{U}$  where the columns are vectors of length  $m \times n$  where  $n$  is the number of temporal measurements and  $n$  the number of spatial measurements. In our feature library we now include spatial derivative terms such as  $\mathbf{U}_{xx}$  and  $\mathbf{U}\mathbf{U}_x$  to represent typical PDE terms. The regression problem is then

$$\mathbf{U}_{t,j} = \Theta(\mathbf{U})\xi_j \quad (6)$$

where subscript  $t, j$  represents the time derivative of  $\mathbf{U}$  for the  $j^{\text{th}}$  state.

A primary limitation of SINDy as expressed in Equation (6) is the use of finite-differencing in approximating spatiotemporal derivatives. Even extremely low amplitudes of noise have been noted to cause substantial errors in the identification of PDEs (Rudy *et al.* 2017). This issue is further compounded by the presence of nonlinear product terms in the feature library which conspire to violate the linear regression assumption of additive Gaussian noise (Fung *et al.* 2024). The effect of noise can be ameliorated by using the weak form of PDEs (Gurevich *et al.* 2019). In particular, a weak form of SINDy was introduced by Messenger & Bortz (2021).

The advantage of the weak form lies in the ability to transfer high-order derivatives from the state variables  $\mathbf{u}$  on to a weight function  $\mathbf{w}$  with known form and well defined derivatives. Equation (5) is multiplied by  $\mathbf{w}$  and each term in the library is integrated over  $K$  randomly sampled subdomains of volume  $\Omega_k$  for  $k \in [1, 2, \dots, K]$ . The optimisation is then expressed as

$$\mathbf{q}_{0,j} = \sum_{n=1}^N c_{n,j} \mathbf{q}_n = \mathbf{Q} \mathbf{c}_j \quad (7)$$

where  $\mathbf{Q} = [\mathbf{q}_1, \dots, \mathbf{q}_N]$  is the collection of  $N$  different features of the PDE with the form

$$\mathbf{q}_n^k = \int_{\Omega_k} \mathbf{w} \cdot \mathbf{f}_n \, d\Omega_k. \quad (8)$$

We can then perform PDE identification by assuming the form of the PDE is not known, and substituting a selection of candidate function  $\Theta_m$  for  $\mathbf{f}_n$ . This casts Equation (7) as a linear regression problem; i.e. we wish to minimise the residual sum of squared errors of the  $K$  different integrals on each subdomain. The regression is performed over the results of all the  $K$  integrated subdomains at once. Both the number  $K$  of subdomains used and their locations impact the results of regression as has been shown previously (Abramovic, Alves & Greenwald 2022, Gurevich *et al.* 2024). A larger number of subdomains ensures that the data are more diverse and representative, yielding more structurally robust results for the functional form of the governing equations and recovering the coefficients with higher accuracy due to averaging, especially for noisy data (Gurevich *et al.* 2019). The location of subdomains also matters. For instance, choosing the domains that don't overlap ensures linear independence of the rows of the  $\mathbf{Q}$  matrix. On the other hand, the location can also determine which physical effects are important. Poor sampling of the data can lead to models that are less general. For instance, viscous effects might not be picked up if boundary layers are not sampled (Gurevich *et al.* 2024). By using integration by parts on the amenable feature terms  $\mathbf{q}_n^k$  we can transfer

derivatives from  $\mathbf{u}$  to the weight function  $\mathbf{w}$ , thus greatly improving the robustness to noise. In this form weak SINDy can act as a low-pass filter which averages over periodic high-frequency signals if  $\Omega_k$  spans periods of that frequency (Messenger & Bortz 2021).

Despite an increased robustness to noise, weak SINDy is still susceptible, as with any linear regression problem, to correlated terms in the feature library. This presents a general issue for high-dimensional regression problems that despite including some form of regularisation can still lead to models that are nonphysical. This has led to the inclusion of physical constraints that reduce the overall library size. For the weak form, the most general constraints are given by the SPIDER framework (Gurevich *et al.* 2024, Golden *et al.* 2023) (described later), whereby the search is constrained to one of several group equivariant subspaces. While both pySINDy and SPIDER employ both weak formulation and sparse regression, the former requires specific domain knowledge to constrain the search space, unlike the latter. We present the application of both from a standpoint of an end user.

#### 4.1.1. *Mixed-integer sparse regression*

In this paper we make use of a recent addition to pySINDy termed mixed-integer optimiser for sparse regression (MIOSR) developed by Bertsimas & Gurnee (2023). Sparsity is enforced in MIOSR through Specially Ordered Sets of Type 1 (SOS-1) restricting that only one variable in a set can take a nonzero value. By restricting the total number of allowable terms in the system, an answer is found which chooses the most suitable features in the linear regression problem. The solution is found using branch and bound algorithms which partition the feasible solution space into subsets of problems and solve the linear relaxation of the problem at different nodes. This process is continued until a solution with integer coefficients is found that minimises the objective function and provides a solution to a combinatorially hard search problem (Bertsimas & Gurnee 2023). MIOSR relies on modern optimization solvers such as CPLEX<sup>1</sup> or GUROBI<sup>2</sup> and we employ the latter here. Interested readers can refer to the original work by Bertsimas *et al.* (2016) for full details. When MIOSR is applied to all equations at once, the sparsity constraint  $k$  is termed the group sparsity. Otherwise when it is applied to each equation individually it is referred to as target sparsity.

There are three reasons we make use of this optimiser. First, MIOSR out-performs many of the other available optimisers on a series of benchmarking problems outlined by Kaptanoglu *et al.* (2023). It is also the only optimiser that allows the inclusion of hard-constraints which we make use of to eliminate specific library terms. Finally, as sparsity is enforced by limiting the maximum number of allowable terms appearing in a given equation, terms with small coefficients can readily be identified. Given that diffusive terms scale with  $\sim 1/\sqrt{R}$ , the coefficients adorning these terms will be small. The latter two points make the sequentially thresholded least-squares approach as implemented in pySINDy unsuitable for this problem.

#### 4.1.2. *Problem formulation in the pySINDy implementation*

In general when using pySINDy there are two approaches to library construction. The first is to create a general feature library of say, all product terms of the state variables and their derivatives up to an arbitrarily chosen order of polynomial, and then if necessary constrain the resulting library. The second is to create a bespoke library which contains only the exact features required. More details of how to create complex pySINDy libraries are shown in the documentation<sup>3</sup>. While the second approach is appealing, in practise we found this to be challenging to implement specifically in the weak form SINDy as it involves taking many products of the input features and can still result in derivative terms which are not intended.

<sup>1</sup>CPLEX, I.I.: V12. 8: User's manual for cplex. Int. Bus. Mach. Corp. 46(53), 157 (2017)

<sup>2</sup>Gurobi Optimization, LLC: Gurobi Optimizer Reference Manual (2021). <https://www.gurobi.com>

<sup>3</sup>[https://pysindy.readthedocs.io/en/latest/examples/15\\_pysindy\\_lectures/example.html#Part-5:-How-to-build-complex-candidate-libraries](https://pysindy.readthedocs.io/en/latest/examples/15_pysindy_lectures/example.html#Part-5:-How-to-build-complex-candidate-libraries)



The simplest approach in pySINDy is to create a full general product library and remove unwanted feature terms by constraining them. We return to discuss the possible implications of this choice, particularly with respect to the amount of computing memory consumed by pySINDy, in the Discussion section.

Herein, the pySINDy candidate library is constructed from the pressure  $p$ , the temperature  $T$  and each component of the velocity, treated as a separate scalar feature object:  $u_x$  and  $u_z$  for the 2D problems;  $u_x$ ,  $u_y$  and  $u_z$  for the 3D problem. To construct the custom library for 2D Rayleigh-Bénard convection, we have included these four data objects  $p(x, z)$ ,  $T(x, z)$ ,  $u_x(x, z)$  and  $u_z(x, z)$  (4 terms), first-order partial derivatives (8 terms), second order partial derivatives (16 terms, reduced to 12 applying chain rule), products of the four data objects with the first-order partial derivatives (32 terms) and products of the four data objects with the reduced second-order partial derivatives (48 terms). A total of 104 possible library terms includes all the terms that we know appear in the governing equations. Equivalently, the full candidate library for the 3D problem contains 290 possible terms. Once this library has been generated by brute-force, pySINDy, scalar only in its operation, can then seek a relation for a predefined term by sparse regression and optimisation, which in the case of governing equations here is the time derivative for each feature object, e.g.  $\partial_t p$ .

The library vector and vector of data objects together create a matrix of all coefficient possibilities, which we now artificially constrain using knowledge about the problem in order to create a library of physical terms which is more comparable to the manner in which SPIDER generates a library. We take this artificial step in order to guide hyperparameter sweeping using an unconstrained library, as this is the proper test of whether the machine learning can recover the governing equations. We enforce  $\partial_t p = 0$  by explicitly including instruction not to seek a relation for this expression. We apply the knowledge that diffusion only appears in the governing equations in the form of a Laplacian operator, thus reducing 60 second-order terms to only 6. Furthermore, four of these are explicitly ‘switched off’ for each equation and the coefficients of the remaining terms in each equation are interlinked (i.e. enforced to be equal to each other, in for example the inertial terms — utilising knowledge that the equations are vectorial in nature). For the artificial constraint of the library, we choose to apply the incompressibility constraint in the form

$$\partial_x u_x = -\partial_z u_z, \quad (9)$$

removing 15 terms from the  $u_x$  equation and 15 terms from the  $u_z$  equation. Elements of the full matrix of library terms are then interlinked, i.e. enforced to be equal, so as to represent the coefficients of the vector equations. The regression is thus forced to select exactly equal coefficient values for each component of every vector term (e.g., advection, diffusion and pressure term). We have used these artificial choices, justified only by comparison to the known correct model, to construct and constrain the library only in order to guide the subsequent use of unconstrained libraries, as we discuss below. Note that due to symmetry breaking induced by gravity there is no systematic *a priori* way either to choose the library terms or interlink the coefficients of equations describing different components of vectors (or higher-rank tensors) in SINDy, requiring a lot of *ad hoc* assumptions to be made.

When using weak SINDy there are several hyper-parameters and domain choices that must be made. The first is the volume  $\Omega_k$  over which the integration is performed. In the 3D case we define the volume following Reinhold, Gurevich & Grigoriev (2020)

$$\Omega_k = \{(x, y, z, t) : |x - x_k| \leq H_x, |y - y_k| \leq H_y, |z - z_k| \leq H_z, |t - t_k| \leq H_t\} \quad (10)$$

such that the volumes are centred around randomly selected points  $(x_k, y_k, z_k, t_k)$  in the computational domain. We interpolate from 384 Chebyshev grid space points vertically to a uniform 384-point grid spacing, in order to match the uniform domain division applied in the formation of the library. This involves some loss of detail at the boundaries, which we

counter when necessary by increasing the number of uniformly spaced grid points vertically. A further issue is that positive-definite terms can become increasingly large with increasing  $\Omega_k$ , thus presenting scaling issues in the feature library, which degrade the quality of the fit. The total number of these subdomains  $K$  must also be chosen and we have experimented with using between 300 and 1500, though in general more subdomains is more computationally expensive but yields better results. We explore the effect of varying these parameters in the Results section. We hold other parameters constant, typically to their default values. For example, we use a NumPy random seed of 100 and we set the order of the interpolating polynomial to be 6 in the initiation of the weak PDE library.

For hyper-parameters related to the optimiser, MIOSR only has a few that must be selected. The first is  $\alpha$  which relates to the strength of the  $l_2$  regularisation. In general as the allowable sparsity is small we keep  $\alpha$  small. The second is the sparsity - either group or target. If we fit all equations at once then the correct numbers of terms is 15 in total (group), corresponding to 5 for  $u_x$ , 6 for  $u_z$ , 0 for  $p$  and 4 for  $T$  (target = 5,6,0,4). Reducing this beyond these “correct” values can lead to a loss of smaller contributing terms and can bring some understanding of the dominant balance of the equations. For example, one can search for the Euler equations to test the hypothesis that the diffusive terms will be lost first (with target = 3,4,0,2). Increasing this beyond these values can ‘overfit’ spurious extra terms, though this is not necessarily the case as MIOSR only has the requirement that the total number of terms be less than or equal to the total sparsity value. However, increasing the number of allowed terms does produce a more ill-posed regression problem.

#### 4.2. The SPIDER framework

The SPIDER framework has been shown (Gurevich *et al.* 2024) to be able to recover the complete mathematical model of a physical process (channel flow) - governing equations, constraints and boundary conditions. Unlike SINDy and its variants which all use an ad hoc approach to constraining the search space, SPIDER is a complete framework that combines 1) physical assumptions of smoothness, locality and symmetry for systematic construction of a collection of term libraries which define the search space; 2) a weak formulation of PDEs for evaluating the contribution of different terms; and 3) model agnostic sparse regression algorithm for inferring one or more parsimonious equivariant equations from each library.

For our purpose, SPIDER has some important differences to pySINDy. In particular, SPIDER is able to recover not only scalar equations, but also vector equations. Libraries in SPIDER are constructed by combining physical fields  $\{\mathbf{u}, p, \dots\}$  with differential operators  $\{\partial_t, \nabla\}$  using symmetry covariant operations such as tensor products and contractions. In this way, term libraries containing scalars, vectors, or even higher rank tensors can be constructed for model discovery. Symmetries further split libraries into irreducible representations via the construction of projection operators (Cvitanović 2008) when possible.

Following the example of the turbulent channel flow SPIDER analysis (Gurevich *et al.* 2024) we take the scalar pressure field  $p$  and the vector velocity field  $\mathbf{u}$ , add the scalar temperature field  $T$  and combine them with differential operators. To account for the partial symmetry breaking associated with gravity, we add the unit vector  $\hat{\mathbf{z}}$ . Using these objects, we can construct a feature library of possible candidate scalar terms

$$\begin{aligned} \mathcal{L}_0 = \{ & 1, p, T, \nabla \cdot \mathbf{u}, \partial_t p, p^2, p^3, \partial_t T, T^2, T^3, \mathbf{u}^2, \mathbf{u} \cdot \nabla p, \mathbf{u} \cdot \nabla T, \nabla^2 p, \nabla^2 T, \\ & p \partial_t p, T \partial_t p, p \partial_t T, T \partial_t T, \partial_t^2 p, \partial_t^2 T, p(\nabla \cdot \mathbf{u}), T(\nabla \cdot \mathbf{u}), \mathbf{u}^2 p, \mathbf{u}^2 T, \mathbf{u} \cdot \partial_t \mathbf{u} \} \end{aligned} \quad (11)$$

and a second feature library of possible candidate vector terms

$$\begin{aligned} \mathcal{L}_1 = \{ & \mathbf{u}, \partial_t \mathbf{u}, \nabla p, \nabla T, p\mathbf{u}, T\mathbf{u}, (\mathbf{u} \cdot \nabla)\mathbf{u}, \nabla^2 \mathbf{u}, \partial_t^2 \mathbf{u}, u^2 \mathbf{u}, p^2 \mathbf{u}, \\ & T^2 \mathbf{u}, \partial_t \nabla p, \partial_t \nabla T, p \nabla p, p \nabla T, T \nabla p, T \nabla T, \mathbf{u}(\nabla \cdot \mathbf{u}), \\ & \mathbf{u} \cdot (\nabla \mathbf{u}), \nabla(\nabla \cdot \mathbf{u}), p \partial_t \mathbf{u}, T \partial_t \mathbf{u}, \mathbf{u} \partial_t p, \mathbf{u} \partial_t T, p \hat{\mathbf{z}}, T \hat{\mathbf{z}} \} \end{aligned} \quad (12)$$

which can be applied separately in searching for scalar or vector relations. Employing Galilean invariance could reduce the size of the libraries further (Gurevich *et al.* 2024). This should be the approach going forwards.

SPIDER yields a significantly smaller library; the 26-term scalar library forms the search space for any scalar fields, while the 27-term vector library forms the search space for any vector fields. As noted by Gurevich *et al.* (2024), we emphasize that no domain knowledge specific to the problem, aside from the symmetry (rotational and translational) and the choice of variables, has been used in constructing these two libraries, in contrast to many other approaches. It should also be noted that libraries are modest in size compared to an equivalent 104-term library constructed by the brute-force approach in pySINDy for the 2D problem. Inclusion of physical symmetries and constraints can and does reduce these pySINDy libraries, as we have done above, but this is a process that requires deep library understanding (exact knowledge of the ordering of terms) and given the larger library size to be reduced, is naturally more susceptible to human error.

The simplest scalar and vector relations describing pressure, temperature and velocity data (the governing equations) can now be identified by performing a sparse regression using these libraries  $\mathcal{L}_0$  and  $\mathcal{L}_1$ . Similarly to pySINDy, SPIDER uses the weak form of the PDEs following the approach in Gurevich *et al.* (2019) in order to make the regression more robust. In this application, the numerical data contains only noise at the level of numerical accuracy ( $10^{-6}$ ), but even so, terms involving higher-order derivatives, such as  $\nabla^2 p$ ,  $\nabla^2 T$  and  $\nabla^2 \mathbf{u}$  are still sensitive to this noise. Specifically, the SPIDER framework multiplies each equation by a smooth weight function  $w_j(\mathbf{x}, t)$  and then integrates it over a rectangular spatiotemporal domain  $\Omega_i$  of size  $H_x \times H_z \times H_t$  (in 2D) or  $H_x \times H_y \times H_z \times H_t$  (in 3D).

The derivatives are shifted from the data onto the weight function whenever possible via integration by parts. The integrals are then evaluated numerically using trapezoidal quadratures. We use the same weight function forms raised to a power  $\beta$  for the scalar and vector libraries as defined in Gurevich *et al.* (2024). We similarly start from a value of  $\beta = 8$  in our analysis and only vary this if necessary, as this choice ensures that boundary terms vanish and maximises the accuracy of the numerical quadrature along the uniformly gridded dimensions (Gurevich *et al.* 2019). Given that for SPIDER, we maintain the non-uniform grid in the  $z$  direction, increasing  $\beta$  further has no benefit as it only affects the errors of the quadrature, as illustrated in fig. 2 of Gurevich *et al.* (2024).

In this work, we vary the size of the subdomains  $\Omega_i$ , the number of subdomains and the value of  $\beta$  in order to recover the governing equations, as discussed in more detail below.

To summarise the method of Gurevich *et al.* (2024), the repetition of this procedure for a number of domains  $\Omega_i$  contained either within the full dataset or a specific region of interest (e.g. bulk flow or boundary region), constructs a feature matrix, which can be normalised to ensure the magnitudes of all the columns are comparable, the effect of which is to improve accuracy and robustness of the regression if necessary, although we don't find that necessary for the recovery herein. The resulting over-determined linear system is homogeneous and treats all terms in the library on equal terms, in contrast to pySINDy. Complete details of the procedure can be found in Gurevich *et al.* (2024). Note that in the same result as that work, scalar terms are found that correspond to the incompressibility condition  $\nabla \cdot \mathbf{u} = 0$  and its corollaries in the scalar library  $p(\nabla \cdot \mathbf{u})$  and  $T(\nabla \cdot \mathbf{u})$ . Now that the incompressibility condition has been identified, all the terms which involve  $\nabla \cdot \mathbf{u} = 0$  can be pruned from both

the scalar and vector libraries, reducing their complexity even further compared to brute-force approaches. An iterative greedy algorithm (Gurevich *et al.* 2024, Golden 2024) then identifies multiple term relations from this pruned library. Alongside this algorithm, a residual error is calculated; this error describes the weak form of the relations over all  $K$  subdomains. Selecting a final relation from the comparison of reduced sequences formed by repeating the process and dropping one term each time, is based on the choice between the simplicity (i.e. number of terms  $N$ ) and the accuracy quantified by the residuals, a choice which we explore in depth in the next section. Full details of the SPIDER framework have been published elsewhere (Golden *et al.* 2023, Gurevich *et al.* 2024) and we encourage the interested reader to review those works as well as several other relevant earlier studies (Gurevich *et al.* 2019, Reinbold, Gurevich & Grigoriev 2020, Reinbold *et al.* 2021) on which this implementation of SPIDER is based<sup>1</sup>.

## 5. Results

### 5.1. *pySINDy*

We have considered the application of *pySINDy* only to 2D Rayleigh-Bénard convection, owing to memory constraints; it is our finding that *pySINDy*, for this method of application at least, quickly reaches the limits of the available RAM (196Gb) on the nodes of the supercomputing resources we had available to us. The high memory requirements of *pySINDy* for the PDEFIND method in application to 2D and 3D data have been noted in the *pySINDy* documentation, with an example showing that a resolution of  $32 \times 32 \times 32$  was the resolution possible for a 3D reaction-diffusion system<sup>1</sup>. We discuss the possible reasons for this problematic consumption of memory in the Discussion section.

#### 5.1.1. *Hyperparameter sweeping*

Without intuition about which hyperparameter values to choose, the natural start is to perform a sweep across possible values. We set the location of the spatiotemporal domains according to the randomised selection of points detailed above and the division of each domain ( $x$ ,  $z$  and  $t$ ) extent by a constant for each dimension ( $xdiv$ ,  $zdiv$  and  $tdiv$ ). In combination with the number of spatiotemporal domains  $K$ , these constants are limited at the smallest values (resulting in the largest spatiotemporal domains) by the memory capacity available. At the largest values (resulting in the smallest spatiotemporal domains) we limit our investigation to the maximum number of points in each direction for that particular constant (theoretically true for the strong form only).

The aim of sweeping across these hyperparameters is to find reliable values that can be used to recover governing equations from the unconstrained library. We initially set out to recover governing equations from the constrained *pySINDy* libraries. The hope is that in future work, any physical intuition that can be inferred from these values can be applied in the search for unknown properties of the fluid (e.g. new sub-grid-scale turbulence models). To assess the performance of the resulting models, we calculate the predicted root mean-squared errors over the  $K$  subdomains for which the regression problem is formed.

Initially, we consider 2D Rayleigh-Bénard convection at  $R = 10^6$ . In the first three tests cases, the numerical results are interpolated from a Chebyshev grid to a uniform grid with 384 points in the vertical, with the horizontal resolution remaining the same. This is because *pySINDy* assumes a uniformly sampled spatiotemporal grid from the user in the numerical quadrature. Using a subset of the high-resolution time data available, typically 400 points in

<sup>1</sup><https://github.com/mgolden30/SPIDER>

<sup>1</sup>[https://pysindy.readthedocs.io/en/latest/examples/10\\_PDEFIND\\_examples/example.html](https://pysindy.readthedocs.io/en/latest/examples/10_PDEFIND_examples/example.html)

the range  $50 \leq t \leq 54$ , because of the memory-demands, in the first test, we sample between 300 and 1500 spatiotemporal domains from the bulk of the flow - specifically in the region defined on the ranges  $2.60 \leq x \leq 3.60$  and  $0.27 \leq z \leq 0.73$  (see box 1 in Figure 1). This corresponds to a region of the flow containing approximately half of a quasistable periodic convective roll, including the plume and the centre of the roll. In the second test, we sample from the whole of the bulk, i.e. all  $x$  and  $0.27 \leq z \leq 0.73$  (see box 2 in Figure 1). In the third test, we sample only from the lower boundary layer, following the hypothesis that this may be able to isolate the diffusive terms more easily, i.e. from the range  $0 \leq x \leq 4$  and  $0 \leq z \leq 0.13$  (see box 3 in Figure 1). The uniform grid of the first two cases has spacing set by the bulk of the flow, and thus under-resolves the boundary layers. In this case it is necessary to interpolate to a finer grid with spacing determined by the Chebshev grid at the boundary. The accuracy of numerical quadratures required by the weak form is substantially higher for uniform grids (Gurevich *et al.* 2019). Hence, in the fourth test, motivated by reducing the error and improving the accuracy of the equations recovered, we interpolate the non-uniform vertical 384-point grid defined by the Chebyshev polynomials onto a higher resolution uniform grid of 3840 points and then select spatiotemporal domains from the full  $x$  range and from  $0 \leq z \leq 0.026$ .

For all these tests, we have explored the hyperparameter range of  $x$ ,  $z$  and  $t$  divisions with a default of 300 spatiotemporal domains, which we have increased if necessary. In the first test, we have used divisions in  $x$  of ( $xdiv = 8, 10, 12, 14, 16, 18, 20, 22, 24$ ), divisions in  $z$  of ( $zdiv = 3, 6, 10, 13, 16, 20$ ) and divisions in  $t$  of ( $tdiv = 8, 10, 12, 16, 20, 24$ ). For the other tests, the set of values used for  $x$  and  $z$  are scaled by the size of range sampled, such that we maintain as close to the same size of spatiotemporal domains between the tests.

We illustrate the results of a hyperparameter sweeping test in Figure 2. The results for each equation, for each combination of divisions is colour coded by the residual error of fit. Most published applications of SINDy calculate some normalised measure of the coefficient error to assess model performance (or this choice is not discussed at all). We use this approach here, but it is a limited solution in our case as it relies on recovering only the correct equations (and knowing this beforehand to constrain the libraries and be able to compare the result). The only other option available is to integrate the resulting PDEs and assess their performance, which is computationally infeasible for hyperparameter selection. This normalised cumulative coefficient residual error is lowest in the region of small  $xdiv$ ,  $zdiv$  and  $tdiv$ , specifically at  $(xdiv, zdiv, tdiv) = (12, 10, 8)$ . Physically, these correspond to physically large spatial domains ( $1024/12, 384/10$ ) with the longest periods of time evolution ( $400/8$ ). We further find that equivalents of these values are consistent between the first, second and third tests at  $R = 10^6$ , implying that for this method, it is equally possible to recover Navier-Stokes in both the bulk and at the boundary. The fourth test, sampling from the refined boundary layer, was inconclusive suggesting that the region we sampled from, even with enhanced vertical resolution, was not large enough to recover both the viscous terms (which you would expect to dominate) and the advection terms. Further, any errors existing in the data will simply be interpolated to an increased grid resolution and thus still prevent successful recovery. We return to the question of data accuracy later. The governing equations recovered using the constrained library (where we have constrained vector properties of the equations, as well as applied the incompressibility constraint, in order to produce a more physical library) typically lose the diffusive terms first as you move away from this optimal combination, followed by the addition of extra terms which are not found in the true equations. This may be because weak SINDy introduces a smoothing effect if the domain is too large (Fung *et al.* 2024) or normalisation issues are introduced as terms become larger. For smaller integration domain sizes, there may be insufficient smoothing of errors. It is difficult to be conclusive as one thing we have been unable to adjust when the MIOSR method is used within pySINDy is the tolerance of the MIOSR method and we suggest this may be an avenue for future investigation.

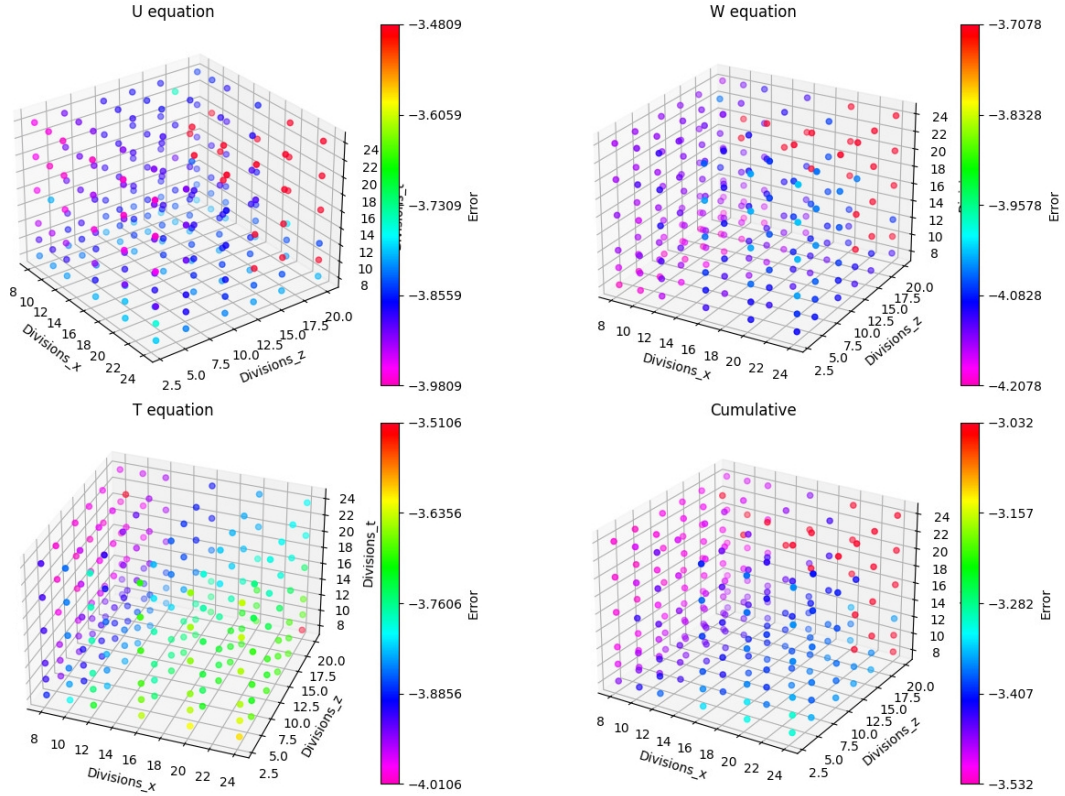


Figure 2. Results of the first pySINDy test at  $R = 10^6$  for 2D Rayleigh-Bénard convection. Sampling spatiotemporal domains from a region of the bulk flow, the figures show the effect of varying the size of the spatiotemporal domains on the resulting residual error (in weak form, over  $K$  subdomains) of the governing equations recovered by the pySINDy implementation. The error shown is the logarithm of the residual sum of squared errors. Specifically (a) visualises the residual error for the  $u_x$  equation, (b) visualises the error for the  $u_z$  equation, (c) visualises the error for the  $T$  equation. Part (d) of the figure combines the residual errors for each equation together with the aim of finding a choice of  $xdiv$ ,  $zdiv$  and  $tdiv$  that corresponds to correct recovery of each governing equation independently; a choice of low  $xdiv$ ,  $zdiv$ , and  $tdiv$  appears to achieve this aim.

$$\begin{aligned}
 (U)' &= \boxed{0.00099995} U_{22} + \boxed{-0.99981655} P_1 + \boxed{0.00099995} U_{11} + \boxed{-0.99979113} WU_2 + \boxed{-0.99979113} UU_1 \\
 (W)' &= 0.99981780 T + \boxed{-0.99981655} P_2 + \boxed{0.00099995} W_{22} + \boxed{0.00099995} W_{11} + \boxed{-0.99979113} WW_2 + \boxed{-0.99979113} UW_1 \\
 (P)' &= 0.00000000 \\
 (T)' &= \boxed{0.00100058} T_{22} + \boxed{0.00100058} T_{11} + \boxed{-0.99920030} WT_2 + \boxed{-0.99920030} UT_1 \\
 msqe &[1.51597724e-04 \ 7.35183276e-05 \ 5.77350269e-02 \ 2.01283110e-04]
 \end{aligned}$$

Figure 3. Results of constrained-library sparse regression using the pySINDy implementation applied to simulation of 2D Rayleigh Bénard convection at a Rayleigh number of  $R = 10^6$ . Terms that are constrained by interlinking and have identical coefficients are indicated by colour boxes; gradient of pressure (green), advection (red and purple), diffusion (blue and yellow). Residual (root mean-squared) error is shown for each of the four equation on the bottom line. The third value (for the pressure equation) can be ignored. We choose to present this in pySINDy output format as an example of the results obtained by this analysis.

It is worth noting that each test required repeated applications of the pySINDy implementation for each combination of  $xdiv$ ,  $zdiv$  and  $tdiv$ , corresponding to different sized spatiotemporal domains. Each test took approximately 24 to 48 hours on a single compute node of the ARC4 facility at the University of Leeds, at one number of  $K$  spatiotemporal domains. Future users may find it useful to note that we found that certain combinations, corresponding to the largest spatiotemporal domains, would attempt to use more than the 196Gb of RAM available and would have to be run on the large memory nodes with 768Gb RAM.

### 5.1.2. Increasing the Rayleigh number $R$

We now increase the value of  $R$  (and hence the level of turbulence) and examine the ability of this pySINDy implementation to recover the Navier-Stokes equation governing velocity

and the heat advection-diffusion equation governing temperature, continuing with the use of a constrained library. As demonstrated in the previous section, recovery of these equations at  $R = 10^6$  was robust when the library was constrained in the manner described above. In Figure 3, we show an example output of our pySINDy analysis. Four equations are shown, all scalar, for the evolution of the two components of velocity, the pressure and the temperature. There is no pressure evolution equation, as expected from the constraints. The equivalent scalar equations following the notation of Equation 1 are

$$\begin{aligned} \frac{\partial u}{\partial t} = & \textcolor{blue}{0.00099995} \frac{\partial^2 u}{\partial z^2} + \textcolor{green}{-0.99981655} \frac{\partial p}{\partial x} + \textcolor{blue}{0.00099995} \frac{\partial^2 u}{\partial x^2} \\ & + \textcolor{red}{-0.99979113} w \frac{\partial u}{\partial z} + \textcolor{red}{-0.99979113} u \frac{\partial u}{\partial x}, \end{aligned} \quad (13)$$

$$\begin{aligned} \frac{\partial w}{\partial t} = & 0.99981780 T + \textcolor{green}{-0.99981655} \frac{\partial p}{\partial z} + \textcolor{blue}{0.00099995} \frac{\partial^2 w}{\partial z^2} \\ & + \textcolor{blue}{0.00099995} \frac{\partial^2 w}{\partial x^2} + \textcolor{red}{-0.99979113} w \frac{\partial w}{\partial z} + \textcolor{red}{-0.99979113} u \frac{\partial w}{\partial x}, \end{aligned} \quad (14)$$

$$\frac{\partial p}{\partial t} = 0, \quad (15)$$

$$\frac{\partial T}{\partial t} = \textcolor{cyan}{0.00100058} \frac{\partial^2 T}{\partial z^2} + \textcolor{cyan}{0.00100058} \frac{\partial^2 T}{\partial x^2} + \textcolor{magenta}{-0.99920030} w \frac{\partial T}{\partial z} + \textcolor{magenta}{-0.99929939} u \frac{\partial T}{\partial x} \quad (16)$$

where the same colour coding has been used to highlight values of coefficients that are enforced to be exactly identical to one another - interlinked - by the constraint of the library.

A repeated set of tests at  $R = 10^8$  has shown similar ability to correctly recover the governing equations, again accurate for a range of hyperparameter spatiotemporal domain values ( $xdiv$ ,  $zdiv$  and  $tdiv$ ) around those optimally found for  $R = 10^6$ . At larger  $R$ , this robust result of the regression becomes less stable, meaning that even with a constrained library, at  $R = 10^{10}$  only the optimal parameters recover the governing equations and at  $R = 10^{12}$ , only the Euler equation is recoverable. Again, this behaviour is consistent between tests 1, 2 and 3 and inconclusive for test 4. This is interesting in of itself, as from physical intuition, natural expectation may expect us to see different behaviour between these tests - we did not see that. The difficulty of recovering governing equations at high  $R$  may be due to the coefficient of the diffusive term being a factor of  $10^6$  smaller than the other coefficients - equation discovery algorithms are known to struggle with a wide numerical range of coefficient values. It should also be noted that the diffusive terms in the boundary layer are the smallest structures and therefore the most difficult to resolve. In this instance we are inclined to conclude that the tolerance of the MIOSR optimiser is set too high by default for this case, but we also return to the effect of our chosen resolution on these machine learning methods later. Future investigation is advised to understand the difference in equation recovery when sampling from different regions of the flow, although we can say that applying a post-computation increase in the number of points vertically by interpolation, simply to provide a larger number of points to sample from for the selection of spatiotemporal domains, does not improve the equation recovery performance; the end-user of machine learning equation recovery techniques should be sure the numerical computations are well-resolved from the outset - a point we return to in later discussion.

### 5.1.3. Unconstrained library regression

It should be noted that with a constrained library, the correct form of each term in the equations is selected in the regression. When using unconstrained libraries, where all possible

```

(U)' = 0.00100425 U_22 + -0.99923014 P_1 + 0.00099672 U_11 + -0.99917831 WU_2 + -0.99950555 UU_1
(W)' = 1.00007174 T + -1.00006861 P_2 + -0.00100302 U_12 + 0.00099892 W_11 + -0.99986125 WW_2 + -1.00037041 UW_1
(P)' = 0.00000000
(T)' = 0.00100773 T_22 + 0.00100044 T_11 + -0.99941317 WT_2 + -1.00108176 UT_1
msqe3
[1.46961159e-04 6.43895751e-05 5.77350269e-02 1.25185292e-04]

```

Figure 4. Results of unconstrained-library sparse regression using the pySINDy implementation applied to simulation of 2D Rayleigh Bénard convection at a Rayleigh number of  $R = 10^6$ . Residual (root mean-squared) error is shown for each of the four equation on the bottom line. The third value (for the pressure equation) can be ignored.

library terms are available, there are some common swaps which appear in the recovered equations. In particular for this incompressible problem, swaps related to the incompressibility condition are common (though of course this is then simply a different correct way of writing the resulting equations — though may lead to a different physical interpretation of the terms in the equations).

Noting that this occurs, with the optimally selected hyperparameters from the constrained fitting, regression with the unconstrained library is able to recover the governing equations at the parameter values which correspond to the minimal error, as shown in Figure 4 for  $R = 10^6$ . A ‘swap’ is notable in the  $u_z$  (W’) equation in the diffusive terms, where  $\partial^2 u_z / \partial z^2$  has been replaced by  $\partial^2 u_x / \partial x \partial z$  which is equivalent through the incompressibility condition. The residual errors are in fact slightly smaller than in the constrained regression case, which shows that each equation is being obtained separately, albeit from the same library. Limited target sparsity was also enforced in the regression at an earlier result than shown in order to see if simpler equations (e.g. the Euler equation) are recovered first and this is indeed the case. It is clear then that in order to recover the correct governing equations with large libraries, if no physical intuition is decipherable from inspection of the flow (a point we return to later) one must first optimise the values of the hyperparameters, for example by using a brute-force repetitive computational test of regression at all values to minimise the residual error.

It is also possible to alter the random selection of the spatiotemporal domain locations and statistically quantify some robustness of the result. We find that this process is effective at Rayleigh numbers of  $10^6$  and  $10^8$ , in that with 100 variations of the random seed initialising locations of selected spatiotemporal domains, the resulting equations recovered are correct more than 75% of the time for  $R = 10^6$  and more than 50% of the time for  $R = 10^8$ . But even with tuned hyperparameters, the regression on an unconstrained library is unsuccessful at  $R = 10^{10}$  and above. More specifically, again it is possible to recover the simpler advection terms robustly e.g. the Euler equation, but the recovery of the diffusion terms, with their smaller coefficients, has been found to be very difficult - impossible at  $R = 10^{12}$ . In future work, variation of the order of the interpolating polynomial may be able to improve on this poor results at high  $R$ .

This is as far as we have been able to go with the pySINDy implementation. Clearly for these kind of complex fluid flows, some physical intuition is crucial for this method to constrain the candidate library of possible terms for the sparse regression. Further, examining the flow may provide some intuition about the optimal selection of hyperparameters (and we explore this and the limits imposed by resolution later). The generalised nature of pySINDy places the onus on the end user to make appropriate choices in these areas before investigation of more nuanced parameters like the MIOSR tolerance and the order of the integrating polynomial - which may in fact have much greater bearings on the quality of the resulting equation recovery. We discuss this further in the subsequent Discussion section.



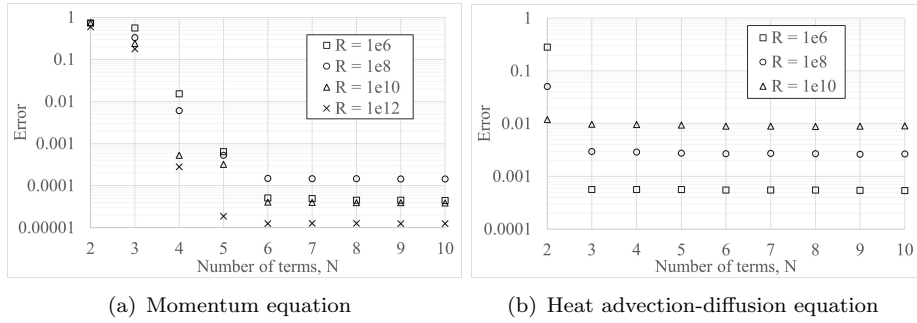


Figure 5. Dependence of the residual on the number of terms  $N$  retained in a recovered relation for the governing (a) momentum equation and (b) heat advection-diffusion equation for 2D Rayleigh-Bénard convection.

## 5.2. SPIDER

### 5.2.1. Governing Equations

Inference of single-term relations in the SPIDER framework requires independent evaluation of all the terms in the corresponding library but does not involve regression (Gurevich *et al.* 2024). We verified that the incompressibility condition (1c) is indeed recovered from the scalar library  $\mathcal{L}_0$  for suitable choices of the sizes of integration domains.

In Figure 5(a) we show the results of the regression analysis performed using the vector library  $\mathcal{L}_1$  pruned for the incompressibility condition (see preceding section) in order to recover the momentum equation (1a). We show the residual error computed as the number of terms allowed in the library is reduced to only 1. The residual error for  $N > 10$  is not shown as it follows the flat trend above  $N = 6$  for the momentum equation and  $N = 3$  for the heat advection-diffusion equation. A natural choice of  $N$ , therefore, would either be 5 or 6 as this is the smallest number of terms at which the error becomes more or less constant. In Table 1 we show the details of the momentum equation recovered by the SPIDER framework for  $R = 10^{10}$ . It is not until four terms are selected that SPIDER recovers an evolution equation and this is reflected in the large reduction in error at this  $N$ . It is reassuring to note that this is the Euler equation. With 5 terms, the SPIDER recovers the Navier-Stokes equation, with very close to the correct coefficient for the diffusive term ( $-10^{-5} \nabla^2 \mathbf{u}$ ). Addition of a 6th term appears to reduce the error further. This extra term, indicated in Table 1 is spurious, but is likely to be fitting a real numerical error, which we discuss further in the next section.

From Figure 5(a), one might naively deduce that the SPIDER framework improves (i.e. produces smaller residuals) with increasing  $R$ . However, note that this masks the adjustment of regression hyperparameters needed to obtain accurate recovery of the momentum equation, which we required for the largest  $R$ . More specifically, at  $R = 10^6$ , we used 1024 spatiotemporal subdomains,  $\beta = 12$  and  $\Omega_i = 128$ . At  $R = 10^8$ , we can reduce  $\Omega_i$  to 64. For  $R = 10^{10}$  we were able to recover governing equation with only 128 subdomains,  $\beta = 4$  and again  $\Omega_i = 64$ . At  $R = 10^{12}$ , the best recovery parameters we found of  $\Omega_i = 128$ ,  $\beta = 4$  and 1024 subdomains were able to recover the Euler equation with 4 terms, but the SPIDER framework consistently selected a  $\partial_t \nabla p$  term before the diffusive term. Given that the coefficient of the diffusive term should be  $10^{-6}$ , perhaps it is no surprise that any method struggles to reproduce such coefficients close to the numerical precision of the simulation. Or, it is possible that SPIDER is telling us something about the quality of the data - we explore this question in the Discussion section. All the same, the recovery of the Euler equation alone by the SPIDER framework for  $R = 10^{12}$  and the robust recovery of Euler and Navier-Stokes equations for  $R = 10^{10}$  is a remarkable performance improvement over pySINDy, at least for this problem and in the manner we have applied both equation discovery methods.

The larger value of  $\Omega_i$  required for the lowest  $R$  laminar flow is not surprising, since the

Table 1. Vector equations recovered by the SPIDER framework from 2D simulation of Rayleigh-Bénard convection at a Rayleigh number  $R = 10^{10}$ , indicative of the same term order recovery with different coefficients for smaller Rayleigh number<sup>a</sup>.

N	Error	Coefficients of terms <sup>b</sup>					
		$\partial_t \mathbf{u}$	$(\mathbf{u} \cdot \nabla) \mathbf{u}$	$\nabla p$	$T \hat{\mathbf{z}}$	$\nabla^2 \mathbf{u}$	$\partial_t \nabla p$
2	0.740	-	-	0.579 <sup>c</sup>	-1 <sup>c</sup>	-	-
3	0.242	-	0.882	0.960	-1	-	-
4	$5.261 \times 10^{-4}$	1	0.999	0.999	-0.999	-	-
5	$3.219 \times 10^{-4}$	0.999	1	1	-0.999	$-1.023 \times 10^{-5}$	-
6	$4.048 \times 10^{-5}$	1	1	1	-0.999	$-1.006 \times 10^{-5}$	$-5.112 \times 10^{-4}$

<sup>a</sup>Whilst recovery of the 4-term Euler equation is consistent across all  $R$ , this table is not indicative of recovering the Navier-Stokes equation for  $R = 10^{12}$ . Please see the text for further explanation.

<sup>b</sup>The sign of the terms here is shown as if everything was moved to the left-hand side of the momentum equation i.e.  $\partial \mathbf{u} / \partial t + \dots = 0$ .

<sup>c</sup>The results produced by the SPIDER framework do indicate a difference between exact integers and decimals.

structures of the laminar flow are large convective rolls and this larger  $\Omega_i$  will sample larger regions of the flow in both space and time. Whilst we have presented results with varying  $\beta$ , in reality the effect of varying this parameter with Fourier-Chebyshev data is small compared to the effect of variation in the number of subdomains and very small compared to the effect of variation of subdomain sizes. Since  $\beta$  would only be expected to improve the regression in the  $x$  direction, then this is no surprise.

In Figure 5(b), we show the results of the regression analysis performed using the scalar library  $\mathcal{L}_0$  pruned for the incompressibility condition and also for time derivatives of  $p$  (akin to deselecting the  $\partial p / \partial t$  equation in the pySINDy libraries) in order to recover the heat advection-diffusion equation (1b). The residual error goes constant from  $N = 3$  terms and it is reassuring to see that the 3-term equation recovered by SPIDER for Rayleigh numbers  $10^6$ ,  $10^8$  and  $10^{10}$  is the correct heat advection-diffusion equation, as shown in Table 2. In this analysis, we used 1024 subdomains and  $\beta = 8$  for all  $R$ . We also set  $\Omega_{x,z} = 64$  and  $\Omega_t = 128$  for both  $R = 10^6$  and  $R = 10^8$ . For  $R = 10^{10}$  we found it necessary to reduce the size of the subdomains to  $\Omega_i = 48$ , indicative of the smaller scale more turbulent structure and thinner boundary layer at this  $R$ . It is noteworthy that despite wide investigation, including converting the vertical resolution from 384 points in a Chebyshev grid to 1024 and 2048 points on a Fourier grid and then experimenting with varying  $\Omega_i$  and  $\beta$ , we have only been able to recover a heat advection equation at  $N = 2$  (and even then only with a reduced scalar library that removes other time derivative terms than  $\partial T / \partial t$ ), but never the heat advection-diffusion equation for larger numbers of terms; the residual error of this is not shown in Figure 5 as it is 0.01 for  $N \geq 2$ . Similarly to the vector equation, where more coefficients are tied together across the vector components, thus possibly making the regression more robust, the identification of the diffusive term with a coefficient close to numerical accuracy is clearly at (and beyond for  $R = 10^{12}$ ) the limit of the algorithms for this data. We also limited the analysis to the boundary layer only, but were still unable to recover the full equation. One might also note that the flow is also highly turbulent at this  $R$  and that this incoherence and short correlation lengths and times might pose difficulty for the ML methods, but as we shall demonstrate with three-dimensional simulations, this does not seem to affect the capability of the SPIDER framework to recover the governing equations. In fact, in three dimensions, the accuracy of the recovery improves for both the Navier-Stokes and heat advection-diffusion equations at  $R$  values which result in a turbulent flow, as we discuss next.

Figure 6(a) presents the results of the regression analysis performed using the vector library  $\mathcal{L}_1$  in order to recover the momentum evolution equation in three dimensions. In contrast to the two-dimensional analysis, this time the 4-term Euler equation and 5-term Navier-Stokes

Table 2. Scalar equations recovered by the SPIDER framework from 2D simulation of Rayleigh-Bénard convection at a Rayleigh number  $R = 10^{10}$ , indicative of the same term order recovery with different coefficients for smaller Rayleigh number.

N	Error	Coefficients of terms <sup>a</sup>			
		$\partial_t T$	$(\mathbf{u} \cdot \nabla)T$	$\nabla^2 T$	$T^2$
2	$1.191 \times 10^{-2}$	0.997	1	-	-
3	$9.694 \times 10^{-3}$	0.997	1	$-1.009 \times 10^{-5}$	-
4 <sup>b</sup>	$9.613 \times 10^{-3}$	0.997	1	$9.814 \times 10^{-6}$	$1.598 \times 10^{-3}$

<sup>a</sup>The sign of the terms here is shown as if everything was moved to the left-hand side of the momentum equation i.e.  $\partial T / \partial t + \dots = 0$ .

<sup>b</sup>At  $N = 4$ , an anti-diffusive term is recovered, along with a spurious  $T^2$  term, demonstrating that care has to be taken to physically interpret the recovered results for reasonable solution to the observed problem.

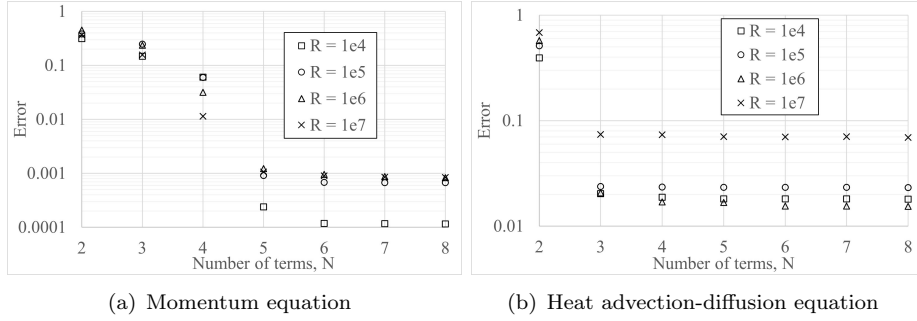


Figure 6. Dependence of the residual on the number of terms  $N$  retained in a recovered relation for the governing (a) momentum equation and (b) heat advection-diffusion equation for 3D Rayleigh-Bénard convection.

Table 3. Parameters of the vector regression analysis used for the application of the SPIDER framework to simulations of 3D Rayleigh-Bénard convection.

$R$	$N_{windows}$	$\beta$	$H_x$	$H_y$	$H_z$	$H_t$
$10^4$	512	8	32	32	64	64
$10^5$	512	8	32	32	64	64
$10^6$	256	4	32	32	32	32
$10^7$	256	4	32	32	32	32

equation are recovered before any other expression for the whole range of  $R$  examined from  $10^4$  to  $10^7$ , which again covers the laminar, transitional and turbulent regimes. The regression parameters are shown in Table 3. It was possible during this analysis to keep the regression parameters fairly consistent, so as to be able to examine the effect of  $R$  on the residual error and it can be seen from Figure 6(a) that a smaller residual error corresponds to a smaller  $R$ , or in other words a more laminar flow pattern with larger structures, which is more coherent and correlated in both space and time, is easier to recover by these methods. This is perhaps not a surprising result - that such an algorithm would have less difficulty with a smoother, less turbulent flow - but interesting to note and reassuring that physical intuition is aligned with the SPIDER framework.

Figure 6(b) presents the results of the regression analysis performed using the scalar library  $\mathcal{L}_0$  in order to recover the heat advection-diffusion equation for three dimensional convection. In an improvement over the analysis of the 2D Rayleigh-Bénard convection data, here the 3-term heat advection-diffusion equation is robustly recovered at all  $R$ . Regression parameters are held constant at 1024 subdomains,  $\beta = 4$  and  $\Omega_i = 32$  for  $R = 10^4$ ,  $R = 10^5$  and  $R = 10^6$  and the residual error is consistent across all these values, albeit higher than for

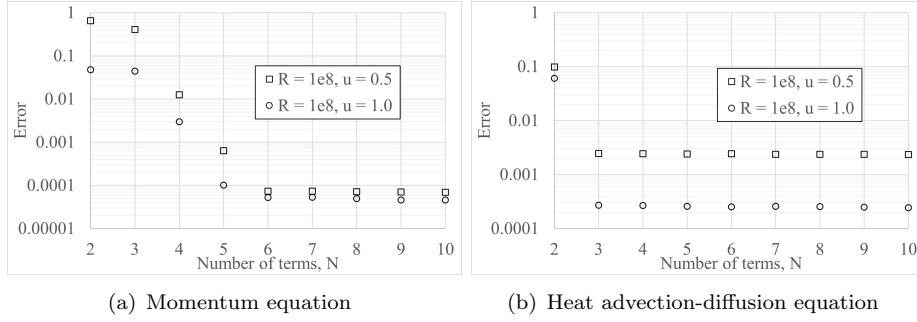


Figure 7. Dependence of the residual on the number of terms  $N$  retained in a recovered relation for the governing (a) momentum equation and (b) heat advection-diffusion equation for 2D planar convective Couette flow.

two-dimensional convection. In order to recover the correct equation and coefficients for the simulation of 3D convection at  $R = 10^7$ , 2048 subdomains, a value of  $\beta = 8$  and  $\Omega_i = [16, 16, 32, 32]$  were required and even then the residual error is far from ideal. Turbulence in the flow does clearly make the regression analysis more difficult, but unsurprisingly there is also a distinct cut off in the ability of machine learning methods as the numerical accuracy of the data is reached.

We show the results of the regression analysis performed using the same libraries applied to the simulated data of 2D planar convective Couette flow in Figure 7. Similarly to the previous two cases, the SPIDER framework is again able to robustly recover the 4-term Euler equation and the 5-term Navier-Stokes equation for the momentum evolution and the 3-term heat advection-diffusion equation before including other terms. These analyses have both used 1024 subdomains. For the vector analysis  $\beta = 12$  and  $\Omega_i = [64, 64, 64]$  produced better residuals and for the scalar analysis  $\beta = 8$  and  $\Omega_i = [64, 64, 128]$  produced better residuals. The velocity of the top and bottom planes did not seem to affect the regression analysis in the recovery of governing equations.

Gurevich *et al.* (2024) noted that for noiseless data, as we have here, the asymptotic value of the residual is determined by the discretization of the data, which would imply acceptable residual errors on the order  $10^{-3}$ , as in general is consistent with what is observed here.

### 5.2.2. Boundary conditions

The recovery of boundary conditions using the SPIDER framework requires a different approach to the libraries, because the rotational symmetry assumption is broken in 2D and partially broken in 3D - the problem is only invariant with respect to rotations about the normal  $\hat{\mathbf{n}}$  to the boundary. To overcome this problem, we follow the approach of Gurevich *et al.* (2024) and include  $\hat{\mathbf{n}}$  in constructing a library  $\mathcal{L}_{\mathbf{u}}$  of terms that transform as vectors, whilst excluding time derivatives. Similarly, to account for the symmetry breaking associated with the wall motion, we include the unit vector  $\hat{\mathbf{x}}$  in that direction. Finally, we exclude the scalar fields  $p$  and  $T$  which yields

$$\mathcal{L}_{\mathbf{u}} = \{\hat{\mathbf{n}}, \mathbf{u}, \nabla(\mathbf{u} \cdot \hat{\mathbf{n}}), (\hat{\mathbf{n}} \cdot \nabla)\mathbf{u}, \hat{\mathbf{x}}\}, \quad (17)$$

where  $\hat{\mathbf{n}} = \pm \hat{\mathbf{z}}$ , depending on whether the top or the bottom boundary is considered. We then split this library into the irreducible representations, an invariant and a covariant, with respect to rotations about  $\hat{\mathbf{n}}$  (corresponding to the normal and tangential components, respectively), by applying the projection operators  $P_{\perp} = \hat{\mathbf{n}}\hat{\mathbf{n}}$  and  $P_{\parallel} = \mathbb{1} - \hat{\mathbf{n}}\hat{\mathbf{n}}$ . This yields the following separate libraries for the velocity

$$\begin{aligned} \mathcal{L}_{\parallel} &= \{P_{\parallel}\mathbf{u}, P_{\parallel}\nabla(\mathbf{u} \cdot \hat{\mathbf{n}}), P_{\parallel}(\hat{\mathbf{n}} \cdot \nabla)\mathbf{u}, \hat{\mathbf{x}}\}, \\ \mathcal{L}_{\perp} &= \{\hat{\mathbf{n}} \cdot \mathbf{u}, 1, \hat{\mathbf{n}} \cdot \nabla(\mathbf{u} \cdot \hat{\mathbf{n}}), \hat{\mathbf{n}} \cdot (\hat{\mathbf{n}} \cdot \nabla)\mathbf{u}\}. \end{aligned} \quad (18)$$

In 2D, these libraries reduce to the components of each field and the derivatives of the components either parallel or perpendicular to the boundary. A scalar library  $\mathcal{L}_T$  for the temperature field  $T$  can be constructed in a similar fashion

$$\mathcal{L}_T = \{1, T, (\hat{\mathbf{n}} \cdot \nabla)T, (\hat{\mathbf{x}} \cdot \nabla)T\}. \quad (19)$$

Only data on the boundary is sampled, effectively selecting a physical profile (for 2D data) or slice (for 3D data) which has variation with time. Again, a number of spatiotemporal subdomains are sampled, typically 256, of a specific size, typically  $\Omega_i = 64$ .  $\beta = 4$  is used. As integration in the wall-normal direction cannot be performed for these samples, a finite differencing of the data has to be performed on the full data and stored, before the original data arrays and the arrays of their derivatives are reduced to obtain a profile or slice. In application to the Rayleigh-Bénard convection problems and specifically only the solid boundaries at  $z = 0$  and  $z = 1$ , the correct temperature and stress-free velocity boundary conditions are recovered *for all  $R$  in both 2D and 3D*. In application to the 2D planar convective Couette flow problem, again the correct temperature and velocity no-slip (fixed velocity of 0.5 or 1.0) boundary conditions are recovered. This demonstrates another advantage of SPIDER in being able to recover boundary conditions, as well as governing equations and constraints.

## 6. Discussion

It has been difficult to find other works which are as revealing about finding the hyperparameters which work well for pySINDy as we have been herein. This is not a simple process and in order to perform the methodical hyperparameter sweeps we have performed above, requires access to computing resources with significant amounts of memory. Further, assessing the results of these sweeps is also tricky.

The key difference between pySINDy and SPIDER is physical constraints. In the pySINDy implementation, the brute force approach combines everything together and the end user is left to use the resulting large library or manually reduce this library in a non-simple manner. The linking of terms across the regression matrix to make coefficients of vectors adds another layer of complexity. Extending pySINDy to libraries containing higher-rank tensors while ensuring equivariance is prohibitively difficult. SPIDER crucially relies on the physics to define the library - more specifically the irreducible representations of the symmetry group describing the physical problem, defined by the data and differential operators such as  $\partial_t$  (or  $\partial_t + \mathbf{u} \cdot \nabla$  in the Galilean-invariant case) and  $\nabla$ . This is really the crucial difference between pySINDy and SPIDER that is shown clearly in the size of the respective libraries and that makes SPIDER more intuitive to use, at least for fluid dynamicists such as ourselves.

It is also interesting to reasonably hypothesize that the memory problem we have observed when using pySINDy, even in 2D, may be related to the size of the library. Even with terms ‘disabled’, the column for that term still exists in the matrix and therefore consumes computing memory in the regression calculation. A way to overcome this memory problem in future work may therefore be to only use very custom libraries which mimic the same physical approach as that used in our SPIDER framework. We emphasize that this is not currently a simple task to consider, especially when further interlinking of terms in this library is then required to mimic vector (or even higher-rank) equations. But, we also emphasize, this is our suggested route to overcoming the memory problem we have observed and that is opaquely referred to in pySINDy documentation (see earlier in this work for specific details).

It is interesting to consider how these methods may be used to discover unknown, rather than known, governing equations, constraints and boundary conditions as we have detailed here. In fact, we intend to apply these same methods to the search for turbulent closure models such as Garaud *et al.* (2010) using our insight from this work and that of other authors (Jakhar

*et al.* 2024). In particular, for pySINDy, it is clear that parameter sweeps of the regression hyperparameters do result in finding the best combination of these parameters for the analysis, which can then be used as, for example,  $R$  is increased, as we did herein, or in future may be used to construct the default position for the uninformed turbulence closure analysis. We expect such similar parameter sweeps may be easily done in the future with SPIDER as and when the python library for SPIDER becomes available. This would also be aided by the ability to fit higher order tensors. In combination with careful library selection of suitable terms, e.g. triple correlation velocity terms, this regression tuning for a particular flow will be key to uninformed discovery with either machine learning method used here. Such parameter sweeping with SPIDER as we did with pySINDy, when possible, may fill in the gaps and/or extend the ability to fine tune the regression parameters and solve the open questions/limits of SPIDER above. For any turbulence closure analysis, we remind the interested reader that there is also the question of separating the mean and fluctuating components of the flow, a fuller discussion of which can be found in Jakhar *et al.* (2024).

It is notable that only a certain set of hyperparameters were varied for the pySINDy approach. Throughout the pySINDy analyses, we held the order of the integrating polynomial constant at 6, in order to make the exploration tractable with the resources available as much as anything else. With SPIDER, it was an easier proposition to alter the equivalent  $\beta$  parameter and we did so as detailed above. Future pySINDy work should consider the variation of the order of the integrating polynomial if the four-dimensional hyperparameter exploration is possible.

We have observed that both pySINDy and SPIDER are capable of recovering small spurious terms in the governing equations, likely to be fitting real error. In our experience, this error is either some small numerical error in the fields (common in low order integration/reconstruction schemes) or it is possible that the weak form subdomains are not matched to the length/time scale of the dynamics. We have observed that tuning of the size of the subdomains is key to obtaining the “correct” result and requires investigation for each specific instance of  $R$ , making it difficult to generalise the method for this flow problem and only possible for a specific value of  $R$ . This will be useful to recall as our investigation moves to recovery of unknown equations, specifically the recovery of existing and new turbulence closures. Thankfully we are not dealing with a large degree of numerical noise or incomplete data. The machine learning process we detail may be possible with such data, but we leave that to future work which could be easily investigated from the Dedalus, pySINDy and SPIDER scripts we publish alongside this paper.

It has been emphasized previously (Gurevich *et al.* 2024) that a proper non-dimensionalisation of the data is required. The non-dimensionalisation of the model, chosen here for numerical convenience more than anything else (see Section 2), seems to have been effective for both the machine learning analyses. It is possible that a better non-dimensionalisation, or further a recasting into different coordinates (as noted is particularly effective for certain problems in pySINDy), may improve the performance we have observed here. An exploration of different non-dimensionalisations and such recasting is beyond the scope of this work.

### 6.1. Using domain knowledge to choose subdomain sizes - correlation scales

It should be possible to avoid the kind of hyperparameter sweeping that we have done here, as analysis of the flow can inform the initial choice of the size of the subdomains. In particular, calculation of the correlation length and time of the flow from the data may give some good *a priori* indication of the optimal spatiotemporal domain. That said, in the SPIDER analysis, the box sizes were held constant in terms of the number of grid points - *which crucially allowed the boxes to be physically smaller in the vertical direction closer to the boundaries as an effect*

Table 4. Correlation lengthscales and timescales for the simulations of 2D Rayleigh Bénard convection.

$R$	$x_{corr}$	$z_{corr}$	$\ell_{corr} = (x_{corr}^2 + z_{corr}^2)^{0.5}$	$t_{corr}$
$10^6$	0.49	0.23	0.54	1.07
$10^8$	0.62	0.24	0.67	0.68
$10^{10}$	0.63	0.24	0.67	0.80
$10^{12}$	0.32	0.22	0.39	0.82
Average:	0.51	0.23	0.57	0.84

of the non-uniform spacing of the grid. It is possible that this approach is key to the improved performance we have obtained with SPIDER.

We have calculated the temporal and spatial correlation scales, defined at the point where the normalised autocorrelation function drops from 1 to 0.5 for the first time, from the same data modelling the 2D Rayleigh-Bénard convection as used in the machine learning approaches. We have employed the calculation techniques detailed in Saxton *et al.* (2024) to calculate these correlation scales. The results of this analysis are shown in Table 4. Perhaps unsurprisingly, all of these scales seem relatively constant with respect to  $R$  and we include the average values across  $R$  in the bottom row of the table; this shows that the correct non-dimensionalisation can yield results that are not sensitive to parameter values. The PDFs of these values across the domains are relatively narrow, especially for  $x_{corr}$ . It should be noted that this does support our finding that the same optimal pySINDy hyperparameter set of (12,10,8) worked across varying  $R$ . Dividing the domain size for the machine learning analysis  $(x_{dom}, z_{dom}, t_{dom}) = (4, 1, 4)$  by the optimal hyperparameter set (12,10,8), gives the physical size of the spatiotemporal subdomains: (0.33, 0.1, 0.5). This is not in full agreement, but it can be noted from the range of values explored and limited by memory capacity, we did not go lower than 8 for  $t_{div}$ . The trend with varying  $x_{div}$ ,  $z_{div}$  and  $t_{div}$  in Figure 2 is for the residual error of the machine learning fit to improve (decrease) as the values approach these correlation scales. The comparison with the SPIDER spatiotemporal subdomains is less obvious, as the physical sizes of the boxes varied in  $z$ , but we were typically using  $\Omega_i$  equal to 128 or 64 for 2D Rayleigh-Bénard convection, corresponding to 0.5 or 0.25 in  $x$  and 1.28 or 0.64 in  $t$ , which are pleasingly close to the average correlation time and spatial scales in both cases. On this basis we would suggest that hyperparameter exploration takes the correlation time and spatial scales of the bulk flow as a default starting point for the size of the spatiotemporal subdomains. It may also be necessary to consider the correlation scales in the boundary layer to infer the small terms that scale as  $R^{-0.5}$ .

Gurevich *et al.* (2019) considered the physical and mathematical intuition regarding optimal integration domain size. They found that optimal integration domain size is a balance. Too small a domain and the error is large because the integration domain is too small to effectively average out the influence of noise. Further, the numerical quadrature error becomes large. Too large a domain and the machine learning analysis enters a regime where the error should grow exponentially in the dimensions  $H_x$ ,  $H_y$ ,  $H_z$  and  $H_t$  of the integration domains. The optimal choice is a crossover between these two regimes, which we find herein has a similarity to the correlation scales. The interested reader may also want to consider the recent Handbook of Numerical Analysis Vol. 25, and in particular Chapter 2 (Bortz, Messenger & Tran 2024).

## 6.2. Numerical accuracy

The failure of the machine learning methods to recover all of the terms – and hence all of the physics – contained in the original governing equations raises the important question of whether this is due to a limitation of these methods or the underlying data that is used. More precisely, we should question whether that failure is indicative of the simulations with

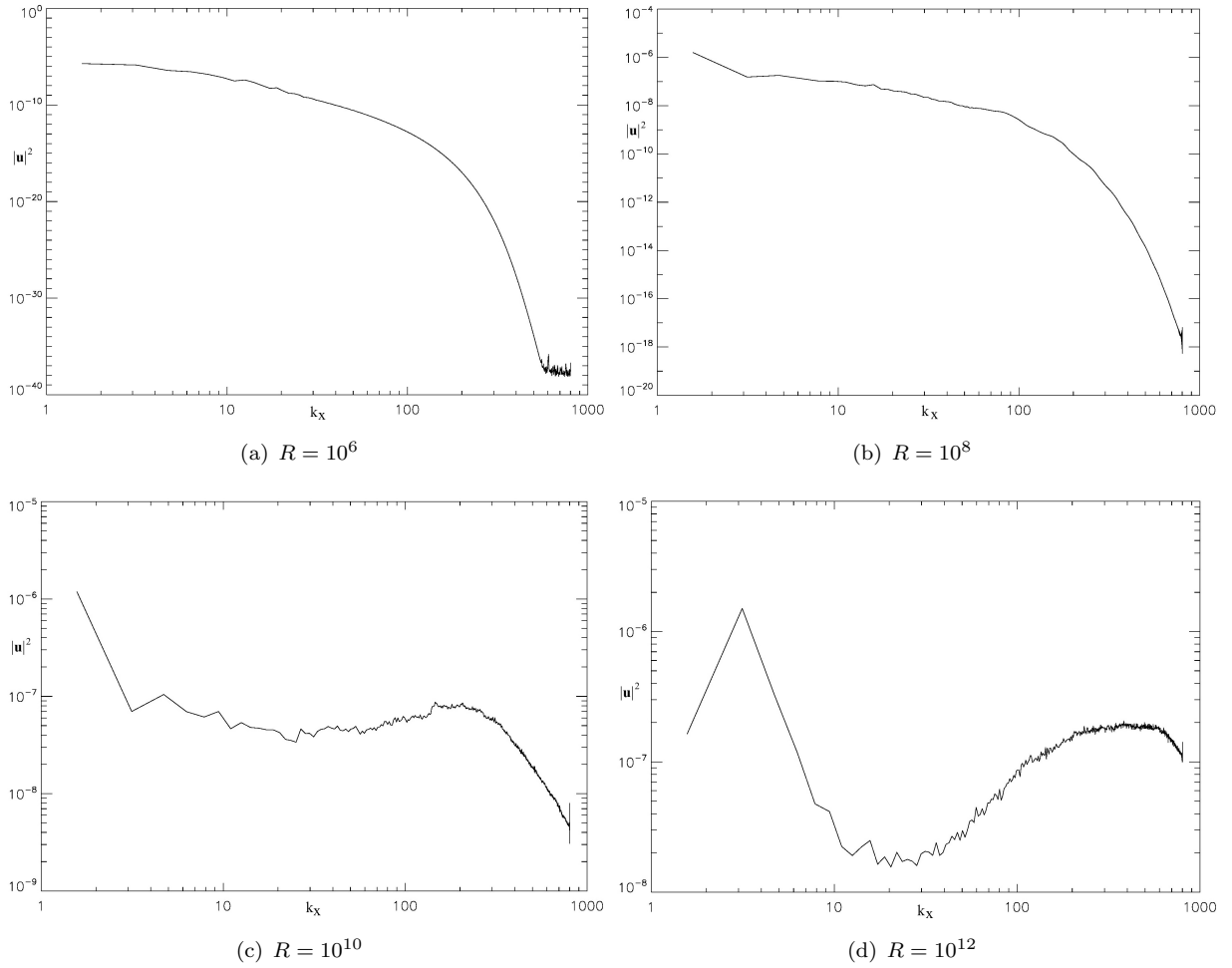


Figure 8. 1D power spectra along profiles in the  $x$  direction ( $k_x$  only) at a height of 10 Chebyshev nodes above the boundary layer for the 2D simulations of Rayleigh-Bénard convection, so as to sample the power spectra of the small-scale dissipative structures in the boundary layer. As can be seen from the top row, the complete power spectra of the boundary layer is captured at Rayleigh numbers of  $10^6$  and  $10^8$ . As can be seen from the bottom row, most of the power spectra at  $10^{10}$  is captured, but at  $R = 10^{12}$  the simulations capture the peak of power spectra in the boundary layer only.

the highest values of  $R$  being sufficiently well resolved. Our choice of Chebyshev polynomials in the vertical direction with the number of cells in the boundary layer matching published DNS simulations (as discussed in Section 3) and tracking of statistics and monitoring of the simulations gave us initial confidence in the quality of the data, but on the other hand the presence of spurious terms in the equation recovery is concerning.

In an attempt to definitively answer this question, noting that the difficulties have been in the recovery of diffusive terms in 2D Rayleigh-Bénard convection, which takes the largest values in the boundary layers, we investigated the resolution of the data in that region. Since the vertical grid spacing in the boundary layer is much finer than the horizontal grid spacing, we focused on the power spectra along the  $x$  direction at a height just above the boundary. The results are shown in Figure 8. Clearly the boundary layer in the  $R = 10^6$  and  $R = 10^8$  simulations (shown across the top row) is spatially well resolved, accurately capturing the steep gradient of the spectra beyond the peak to many orders of magnitude below peak power in the boundary layer. However, at  $R = 10^{10}$  we see that far less of the steeply dropping spectrum beyond the peak at  $k_x^* \approx 200$  is captured with only 1024 points in the horizontal direction. At  $R = 10^{12}$ , it's now clear that with the same horizontal resolution, DNS does not capture



Table 5. Benefits of either machine learning approach

pySINDy implementation	SPIDER framework
Generalisability to further problems	Specific applicability to tensor PDEs
Flexibility of library generation <sup>a</sup>	Specificity of library generation
Ease of hyperparameter sweeping using pySINDy	Ease of Matlab scripting
Range of optimisers available	Ease of optimiser adjustment
Extensive documentation <sup>b</sup>	Relative high speed
Support group <sup>c</sup>	Interpretable results
	Ability to validate and verify DNS

<sup>a</sup>Although flexibility without guidelines can more of a problem for these complex PDE problems.

<sup>b</sup><https://pysindy.readthedocs.io/en/latest/>

<sup>c</sup><https://github.com/dynamicslab/pysindy/issues>

the structures in the boundary layer corresponding to wavenumbers  $k_x$  greater than the peak  $k_x^* \approx 500$ . With the smallest scales ( $k_x > k_x^*$ ) unresolved in the boundary layer, it is not surprising that the both pySINDy and SPIDER fail or struggle to recover the diffusive terms at these high  $R$ . In fact, it is worth emphasizing that SPIDER was telling us, by recovering Euler rather than Navier-Stokes equations, that the DNS data is under-resolved before we confirmed this for the boundary layer through these power spectra. Future theoretical work in particular may therefore be able to use machine-learning tools as an additional method of validation and verification of simulations to demonstrate that they are indeed accurately resolving everything the governing equations should be generating in the flow. We strongly suggest that any future work explores the resolution question very carefully if the machine learning methods are to prove their true usefulness in discovering new physics, rather than just demonstrating an ability, when carefully tuned, to recover known properties of a particular problem. Spatial resolution can clearly be examined by power spectra not only of the whole flow and bulk flow, but also of horizontal slices in the boundary layer. Dedalus also allows the end-user to track maximum values of the tau terms, which for example relate to the divergence of  $\mathbf{u}$ , and can be used to establish the necessary resolution in any direction using a Chebyshev basis, and we have monitored this to ensure we have resolved the numerical simulations. However, it is not clear that the choice of the Chebyshev basis, which place most of the nodes near the boundaries, is necessarily the wisest approach for fully turbulent simulations where small-scale structure can also be found in the bulk flow region. The DNS results (Zhu et al. 2018) to which we have compared our resolution in Section 3 use the Fourier basis in all directions. It is also not yet clear, at least from this work, how temporal resolution between the ‘snapshots’ that are used in the machine-learning methods may affect their performance, but we suggest this avenue could also be easily explored in future.

### 6.3. Guidance for future end-users

In an attempt to provide helpful guidance to readers for the future work and the application of these methods to other problems, we tabulate some of the advantages of either method in Table 5.

For our purposes, we have found above that either method is capable of generating results, although SPIDER has been easier to apply than pySINDy. The memory problems we have observed with pySINDy may be avoided by a different approach to library generation. The ability to parameter sweep with SPIDER may be possible with command line application of a reduced library. That said, investigation of the results of hyperparameter sweeping requires very careful examination of every recovered set of equations in order to check the model and find optimum hyperparameter combinations. We are aware that a future Python version of SPIDER may also make parameter sweeping easier.

The search for the optimal size of spatiotemporal subdomains may be avoided by the detailed examination of the raw flow data. Optimal parameters for pySINDy clearly show a similarity to the correlation lengths and times we have calculated for the simulations of 2D Rayleigh-Bénard convection. Further investigation may then be able to more thoroughly explore the variation of the order of the integrating polynomial  $p$  for the pySINDy implementation and the same thing in SPIDER, the power of the weight function  $\beta$ . We have found that starting from 8 and exploring the range from 4 to 15 is worthwhile. That said, the uniformity of the gridding can strongly affect the performance on variation of this parameter and conversion of non-uniform grids to uniform grids is worth consideration. Note though that SPIDER's advantage herein may in part be due to effect of the non-uniform vertical grid spacing allowing for resolution of the boundary layers. Finally, it bears repeating that variation of the MIOSR tolerance in the pySINDy implementation of SINDy and in fact any tolerances for these optimisers requires further investigation.

## 7. Summary and future work

In this work, we have applied two machine learning methods to simulated convective fluid flows. In particular, we have applied the Sparse Identification of Nonlinear Dynamics (SINDy) algorithm through the pySINDy implementation and the Sparse Physics-Informed Discovery of Empirical Relations (SPIDER) framework with the aim of equation recovery from the raw data. Both pySINDy and SPIDER have proved able to recover governing equations of the 2D Rayleigh-Bénard convection flow simulated. SPIDER was also able to recover governing equations of the 3D Rayleigh-Bénard convection flow and planar convective Couette flow simulated. All simulated data was generated using the Dedalus PDE framework. However, our method of application has shown that whilst pySINDy and SPIDER are essentially doing the same thing, it is clear that the generalised approach of pySINDy puts it at a disadvantage when examining problems that SPIDER is tailored to from the outset. Specifically, the creation of suitable libraries of possible terms for selection in the sparse regression process is physically intuitive with SPIDER as opposed to combinatorially brute force approach-like with pySINDy. This generation of large libraries with pySINDy followed by the deactivation of many terms in the library due to physical constraints is likely to be presenting itself in the high memory demands of the algorithm as we have applied it, so much so that we were only able to apply pySINDy to the recovery of the governing equations of 2D Rayleigh-Bénard convection at Rayleigh numbers of  $10^6$ ,  $10^8$  and  $10^{10}$ . Sweeping of the hyperparameters used to perform the sparse regression, specifically the size of spatiotemporal subdomains, was possible though and analysis indicates that properties of the flow, specifically correlation lengthscales and correlation timescale should inform the initial selection of these parameters. With SPIDER, we were able to demonstrate the recovery of governing equations, constraints (the incompressibility condition) and boundary conditions for all the fluid flows considered: 2D Rayleigh-Bénard convection at Rayleigh numbers of  $10^6$ ,  $10^8$ ,  $10^{10}$  and  $10^{12}$  (albeit with performance limited at  $R = 10^{12}$  most likely for reasons of numerical accuracy which it seems SPIDER can robustly identify), 3D Rayleigh-Bénard convection at Rayleigh numbers of  $10^4$ ,  $10^5$ ,  $10^6$  and  $10^7$ , and 2D plane convective Couette flow at a Rayleigh number of  $10^8$  with varying moving boundary velocities. In combination with the fact that SPIDER is able to directly recover scalar *and* vector equations, it is clear that it is well-tailored to the search for potential new turbulence closures with the addition of extra library terms (e.g. cubic and quartic derivatives) and higher rank tensor equations, something that we intend to examine in future work as development of these methods allows such capabilities. A harder test of both methods may have been to include such higher derivatives in both libraries and perhaps it is little surprise that a method performs better when more knowledge is applied in the generation of the library. All the same,

we would recommend starting with the SPIDER framework for similar problems to those considered here and using flow properties, specifically the time and spatial correlation scales, to inform the initial selection of spatiotemporal subdomain sizes. Investigation of equation recovery can then focus on the importance of other hyperparameters, such as the order of the integrating polynomial in pySINDy and the equivalent power of the weighting function  $\beta$  in SPIDER, as well as tolerance of the optimising methods. We make available all our Dedalus, pySINDy and SPIDER scripts in the hope that they prove useful to anyone considering this or similar problems in the future.

In conclusion, we look forward to some kind of automation procedure for the pruning and constraining of candidate term libraries for the recovery of governing PDEs, as well as further intuition that can be garnered from the raw data to inform machine learning, as both of these appear key to streamlining our methods and applying them to more complex problems. We also anticipate that the use of such machine learning methods may now open a new avenue to validate and verify DNS in both a qualitative sense (are the equations being solved reconstructed?) and a quantitative sense (what is the residual of the equations which does not rely on a particular discretization scheme?).

## 8. Acknowledgements

This project has received funding from the European Research Council (ERC) under the European Union's Horizon 2020 research and innovation programme (Grant agreement No. D5S-DLV-786780). The calculations for this paper were performed on the University of Leeds ARC4 facility, hosted and enabled through the ARC HPC resources and support team at the University of Leeds, to whom we extend our grateful thanks. We express our thanks to Dr Curtis J Saxton for the application of his correlation length calculation scripts to our data.

## 9. Declaration of interests

The authors are unaware of any conflict of interest.

## 10. Data & Materials Availability

With the intention of making this entire work reproducible and applicable by other researchers to different data in the future, all of the code, model initialisations, libraries, data, instructions for the recreation of the larger datasets and machine learning analysis scripts are available in a data repository accompanying this paper<sup>1</sup> provided by the University of Leeds Research Data Repository Service.

## 11. Author contributions

All authors contributed to the conception and design of this work. Data generation and analysis were performed by Chris Wareing. Initial pySINDy guidance and scripting was co-developed with Alasdair Roy. Initial SPIDER guidance and scripting was co-developed with Matt Golden and Roman Grigoriev. The first draft of the manuscript was written by Chris Wareing and all authors helped with manuscript further development and revision. Steven

---

<sup>1</sup><https://doi.org/10.5518/1577>

Tobias provided critical leadership and guidance. All authors read and approved the final manuscript.

## References

- Abramovic, I., Alves, E.P., Greenwald, M., Data-driven model discovery for plasma turbulence modelling. 2022, *J. Plasma Physics*, 88, 895880604
- Ascher, U.M., Ruuth, S.J. and Spiteri R.J., Implicit-explicit Runge-Kutta methods for time-dependent partial differential equations. 1997, *Applied Numerical Mathematics*, 25 (2-3), 151-167.
- Bertsimas, D., Gurnee, W., Learning sparse nonlinear dynamics via mixed-integer optimization. 2023, *Nonlinear Dynamics*, 111, 6585–6604.
- Bertsimas, D., King, A., Mazumder, R., Best subset selection via a modern optimization lens. 2016, *The Annals of Statistics*, 44 (2), 813-852.
- Bolton, T., Zanna, L., Applications of Deep Learning to Ocean Data Inference and Subgrid Parameterization. 2019, *J. Adv. Model. Earth Syst.*, 11(1), 376-399
- Bortz, D.M., Messenger, D.A., and Tran, A. Chapter 2 - Weak form-based data-driven modeling: Computationally efficient and noise robust equation learning and parameter inference, in *Handbook of Numerical Analysis*, vol. 25, 2024, pages 53-82.
- Brunton, S.L., Proctor, J.L. and Kutz, J.N., Discovering governing equations from data by sparse identification of nonlinear dynamical systems. 2016, *Proceedings of the National Academy of Sciences*, 113(15), 3932–3937.
- Brunton, S.L. and Kutz, J.N., Machine Learning for Partial Differential Equations. 2023, arXiv:2303.17078, <https://doi.org/10.48550/arXiv.2303.17078>
- Burns, K.J., Vasil, G.M., Oishi, J.S., Lecoanet, D. and Brown, B.P., Dedalus: A Flexible Framework for Numerical Simulations with Spectral Methods. 2020, *Physical Review Research*, 2(2), 023068.
- Champion, K., Lusch, B., Kutz, J.N., Brunton, S.L., Data-driven discovery of coordinates and governing equations. 2019, *Proceedings of the National Academy of Sciences*, 116 (45), 22445-22451.
- Chorin, A.J., Hald, O.H., Kupferman, R., Optimal prediction with memory. 2002, *Physica D*, 166, 239-257.
- Cvitanović, P., Group theory: birdtracks, Lie's and exceptional groups. 2008, Princeton University Press, ISBN:978-0-691-11836-9.
- Dubois, P., Gomez, T., Planckaert, L., Perret, L., Machine learning for fluid flow reconstruction from limited measurements. 2022, *Journal of Computational Physics*, 448, 110733.
- Fung, L., Fasel, U., Juniper, M.P., Rapid Bayesian identification of sparse nonlinear dynamics from scarce and noisy data. 2024, arXiv:2402.15357
- Garaud, P., Ogilvie, G.I., Miller, N. and Stellmach, S., A model of the entropy flux and Reynolds stress in turbulence convection. 2010, *MNRAS*, 407, 2451-2467.
- Gao, M.L., Kutz, N.J., Bayesian autoencoders for data-driven discovery of coordinates, governing equations and fundamental constants. 2024, *Proc. R. Soc. A.*, 480, 20230506.
- Golden, M., Grigoriev, R.O., Nambisan, J. and Fernandez-Nieves, A., Physically informed data-driven modeling of active nematics. 2023, *Science Advances*, 9(27), eabq6120.
- Golden, M., Scalable sparse regression for model discovery: the fast lane to insight. 2024, arXiv:2405.09579
- Gurevich, D.R., Reinbold, P.A.K. and Grigoriev, R.O., Robust and optimal sparse regression for nonlinear PDE models. 2019, *Chaos*, 29(10), 103113.
- Gurevich, D.R., Golden, M.R., Reinbold, P.A.K. and Grigoriev, R.O., Learning fluid physics from highly turbulent data using sparse physics-informed discovery of empirical relations (SPIDER). 2024, *Journal of Fluid Mechanics*, 996, A25.
- Jakhar, K., Guan, Y., Mojgani, R., Chattopadhyah, A. and Hassanzadeh, P., Learning closed-form equations for subgrid-scale closures from high-fidelity data: promises and challenges. 2024, *Journal of Advances in Modeling Earth Systems*, 16, e2023MS003874.
- Kaheman, K., Kutz, J.N., Brunton, S.L., SINDy-PI: a robust algorithm for parallel implicit sparse identification of nonlinear dynamics. 2020, *Proc. R. Soc. A: Math. Phys. Eng. Sci.*, 476 (2242), 20200279.
- Kaptanoglu, A.A., Callahan, J.L., Aravkin, A., Hansen, C.J., Brunton, S.L., Promoting global stability in data-driven models of quadratic nonlinear dynamics. 2021, *Phys. Rev. Fluids*, 9 (6), 094401.
- Kaptanoglu, A.A., Zhang, L., Nicolaou, Z.G., Fasel, U., Brunton, S.L. Benchmarking sparse system identification with low-dimensional chaos. 2023, *Nonlinear Dyn.*, 111, 13143–13164.
- Marston, J.B. and Tobias, S.M. Recent Developments in Theories of Inhomogeneous and Anisotropic Turbulence 2023, *Annual Review of Fluid Mechanics*, 55, 351-375
- Messenger, D.A. and Bortz, D.M., Weak SINDy for Partial Differential Equations. 2021, *J. Comp. Phys.*, 443, 110525
- Moser, R.D., Haering, S.W. and Yalla, G.R., Statistical Properties of Subgrid-Scale Turbulence Models. 2021, *Ann. Rev. Fl. Mech.*, 53, 255-286
- Reinbold, P.A.K. and Grigoriev, R.O., Data-driven discovery of partial differential equation models with latent variables. 2019, *Physical Review E*, 100(2), 022219.
- Reinbold, P.A.K., Gurevich, D.R. and Grigoriev, R.O., Using noisy or incomplete data to discover models of spatiotemporal dynamics. 2020, *Physical Review E*, 101(1), 010203(R).

- Reinbold, P.A.K., Kageorge, L.M., Schatz, M.F. and Grigoriev, R.O., Robust learning from noisy, incomplete, high-dimensional experimental data via physically constrained symbolic regression. 2021, *Nature Communications*, 12, 3219.
- Rudy, S.H., Brunton, S.L., Proctor, J.L. and Kutz, J.N. Data-driven discovery of partial differential equations. 2017, *Science Advances*, 3(4), e1602614, 2017.
- Saxton, C.J., Marston, J.B., Oishi, J., Tobias, S.M., Ordering of time scales predicts applicability of quasilinear theory in unstable flows 2024, *Journal of Fluid Mechanics*, 998, A37.
- Schaeffer, H., Tran, G. and Ward, R., Extracting Sparse High-Dimensional Dynamics from Limited Data. 2018, *SIAM Journal on Applied Mathematics*, 78 (6), 3279-3295.
- de Silva, B.M., Champion, K., Quade, M., Loiseau, J., Kutz, J.N., Brunton, S.L., pySINDy: A Python package for the sparse identification of nonlinear dynamical systems from data. 2020, *Journal of Open Source Software*, 5(49), 2104.
- Véras, P., Balarac, G., Métais, O., Georges, D., Bombenger, A., Reconstruction of numerical inlet boundary conditions using machine learning: Application to the swirling flow inside a conical diffuser 2021, *Physics of Fluids*, 33, 085132.
- Zanna, L., Bolton T., Data-Driven Equation Discovery of Ocean Mesoscale Closures. 2020, *Geophysical Research Letters*, 47, e2020GL088376
- Zhu, X., Mathai, V., Stevens, R.J.A.M., Verzicco, R., Lohse, D., Transition to the Ultimate Regime in Two-Dimensional Rayleigh-Bénard Convection. 2018, *PRL*, 120, 144502